International Journal of Nanomedicine

Dovepress
Taylor & Francis Group

Open Access Full Text Article

ORIGINAL RESEARCH

Programmed Synergistic Photochemotherapy and Immune Activation of Triple Negative Breast Cancer Using Anti-PD-L1 Antibody-Conjugated Multifunctional Nanocapsules

Zhiqiang Lin[1,*], Hui Jiang[1,*], Yingying Zhou[2], Li Xu[1], Lixin Jiang[1], Jing Du[1]

[1]Department of Ultrasound, Renji Hospital, Shanghai Jiao Tong University School of Medicine, Shanghai, 200127, People's Republic of China; [2]Department of Ultrasound, Zhabei Central Hospital, Shanghai, 200070, People's Republic of China

*These authors contributed equally to this work

Correspondence: Lixin Jiang; Jing Du, Email jinger_28@sina.com; beautydujing@163.com

Purpose: Triple-negative breast cancer (TNBC) is prone to relapse and metastasis due to the immunosuppressive state of the tumor microenvironment and limited exposure to relevant antigens, and chemotherapy alone has poor efficacy. We have developed a novel theranostic nanoplatform to address these problems: multifunctional nanocapsules (NCs) with a PD-L1-mediated gold shell induce immunogenic cell death (ICD) to remodel the immune microenvironment. PD-L1 and NLG919 dual immune checkpoints are programmed to synergistically sensitize photothermal therapy and chemotherapy, and photoacoustic imaging (PAI) is used to visualize and localize TNBC tissues for identification.

Methods: DOX-NLG919@PLGA@Au-antiPD-L1 NCs (DNPA-aPD-L1 NCs) were prepared using an improved single emulsion water-in-oil (O/W) solvent evaporation method, electrostatic adsorption, gold seed surface-induced crystallization reduction method, and carbodiimide method. A series of animal models were established to focus on the in vivo PAI of NCs, the effects of photochemotherapy combined with immunotherapy and antitumor therapy, ICD induced by NCs, the metabolic distribution of NCs, and toxicity tests.

Results: This project successfully constructed gold nanoshell-PLGA core NCs with PD-L1 antibody co-loaded with chemotherapeutic drugs doxorubicin and indoleamine 2,3-dioxygenase inhibitor NLG919. Laser-triggered release of DOX, NLG919, and photothermal therapy can synergistically induce immunogenic cell death (ICD), thereby enhancing tumor immunogenicity, inhibiting IDO, and reshaping the tumor immune microenvironment. This can effectively eliminate the primary TNBC lesions, inhibit recurrence and metastasis, significantly prolong the survival of tumor-bearing mice, and NCs have good in vivo biosafety. This diagnostic and therapeutic agent can be used for photochemotherapy, immunotherapy, and PAI to visualize and identify TNBC.

Conclusion: The photochemotherapy mediated by the DNPA-aPD-L1 NCs we developed, combined with tumor microenvironment remodeling and immune activation, shows great promise for the diagnosis and treatment of TNBC.

Keywords: triple-negative breast cancer, AuNPs, PD-L1 blockade, photochemotherapy, photoacoustic imaging

Introduction

Triple-negative breast cancer (TNBC) is characterized by a high rate of recurrence and distant metastasis and a low overall survival rate,[1] resulting in a poor clinical prognosis. TNBC patients exhibit a suboptimal response to chemotherapy and are susceptible to early recurrence and metastasis. This phenomenon can be attributed, at least in part, to the immunosuppressed state of the tumor microenvironment, which is incapable of effectively monitoring and eradicating the tumor. Moreover, the restricted exposure of tumor-associated antigens to the immune system enables cancer cells to evade detection and elimination.[2–4] This underscores the pressing need to explore novel treatment modalities.

https://doi.org/10.2147/IJN.S539732
Received: 12 May 2025
Accepted: 30 September 2025
Published: 8 January 2026

Photothermal therapy (PTT) employs the heat generated by near-infrared (NIR) laser irradiation to induce the destruction of tumor cells.[5,6] Its applications extend beyond thermal ablation of tumors, encompassing its noteworthy capacity for light-controlled drug release.[7] When used in conjunction with chemotherapy, it has been observed to markedly enhance antitumor efficacy, with the two methods demonstrating a synergistic effect in terms of enhancing sensitivity.[8–10] The heat produced has been shown to enhance the antitumor efficacy of chemotherapeutic agents and stimulate the immune system, thereby promoting the release of numerous cytokines that enhance antitumor effects and reduce the systemic toxic side effects of chemotherapy.[11] Additionally, the process has been observed to reduce or reverse multidrug resistance.[12,13] The combined application of photochemotherapy (photothermal therapy + chemotherapy) is a promising comprehensive treatment mode for TNBC and is also a current research hotspot.[14] However, the conventional photochemotherapy technique exhibits the following limitations: (1) The majority of these treatments are non-targeted, lacking effective targets for imaging recognition and treatment; (2) The immune microenvironment of tumor tissue is suppressed, and the photothermal effect produced after near-infrared laser irradiation has limited killing effect on cancer tissue and cannot control recurrence and distant metastasis.[1] Therefore, the identification of new specific molecular targets to achieve in vivo visualization and precise, effective photochemotherapy combination therapy for TNBC is a critical bottleneck that urgently needs to be addressed. TNBC lacks effective imaging and therapeutic targets, and programmed death ligand 1 (PD-L1) is significantly overexpressed in TNBC.[15–19] Several studies have confirmed that blocking the PD-L1 pathway with PD-L1 antibodies (aPD-L1) can effectively reverse the immunosuppressive tumor microenvironment, restore T-cell antitumor activity, and enhance the antitumor effects of the body's immune system, making it a potentially effective checkpoint and molecular imaging target for immunotherapy. However, monotherapy may not provide optimal results. Combination therapy that targets multiple antitumor immune pathways to induce synergistic antitumor immunity may be more effective in controlling TNBC growth, recurrence, and metastasis.[20–22] The induction of immunogenic cell death (ICD) has emerged as a novel strategy for tumor immunotherapy. However, the effective triggering of ICD remains a significant challenge. Studies have identified a potential synergy between the anthracycline chemotherapeutic drug DOX and photothermal effects, which can enhance the immunogenicity of dead tumor cells induced by ICD. The process of ICD in cancer cells leads to the release of immune stimulatory molecules, such as high mobility group box 1 (HMGB1), calgranulin (CRT), and adenosine triphosphate (ATP) into the tumor microenvironment.[23,24] These molecules serve as danger signals, inducing the release of damage-associated molecular patterns and the exposure of tumor-associated antigens.[25] Indoleamine-2,3-dioxygenase (IDO) is a special type of checkpoint, and its inhibitors are small-molecule drugs that can be used as regulators to suppress the tumor microenvironment.[26] IDO inhibitors (IDOi) have been shown to alleviate immunosuppression within the tumor microenvironment, thereby inducing the host immune system. This property renders IDOi a promising candidate for application in checkpoint blockade. Among the IDO inhibitors, NLG919 is a novel drug candidate with potential immunomodulatory and antitumor activities.

In the early stage, our research group successfully prepared gold nanoparticles (AuNPs) using chemical reduction method.[27,28] AuNPs have been shown to possess the capacity to absorb light efficiently and convert it into heat energy, thereby inducing effective destruction of tumor cells.[29] Gold nanoclusters, defined as a group of gold atoms ranging from a few to several hundred, have garnered significant attention in the field. They possess a relatively stable multi-nuclear aggregate structure, are small in size, water-soluble and biocompatible.[30–34] Consequently, gold nanoclusters find extensive application in biological imaging, disease diagnosis and cancer treatment. Functional gold nanogranule shells were formed on the surface of poly(lactic-co-glycolic acid) (PLGA) core nanoparticles via electrostatic adsorption and surface seeding, effectively converting photonic energy into photoacoustically induced sound waves for photoacoustic molecular imaging (PAI).

A recent study reported that NLG919 and PD-L1 blockade synergistically promote ICD-triggered immune responses,[35] and confirmed that the combination of photothermal therapy, IDO inhibition, and PD-L1 blockade can effectively inhibit the growth of distant tumors of colon cancer. In light of these findings, we have conceptualized a novel nanodiagnostic and therapeutic platform to address these existing problems: The nanodiagnostic platform consists of gold-shelled multifunctional NCs conjugated with aPD-L1, containing DOX and NLG919 drugs, which are triggered by photothermal effects to synergistically enhance the induction of ICD to improve tumor-associated antigen exposure,

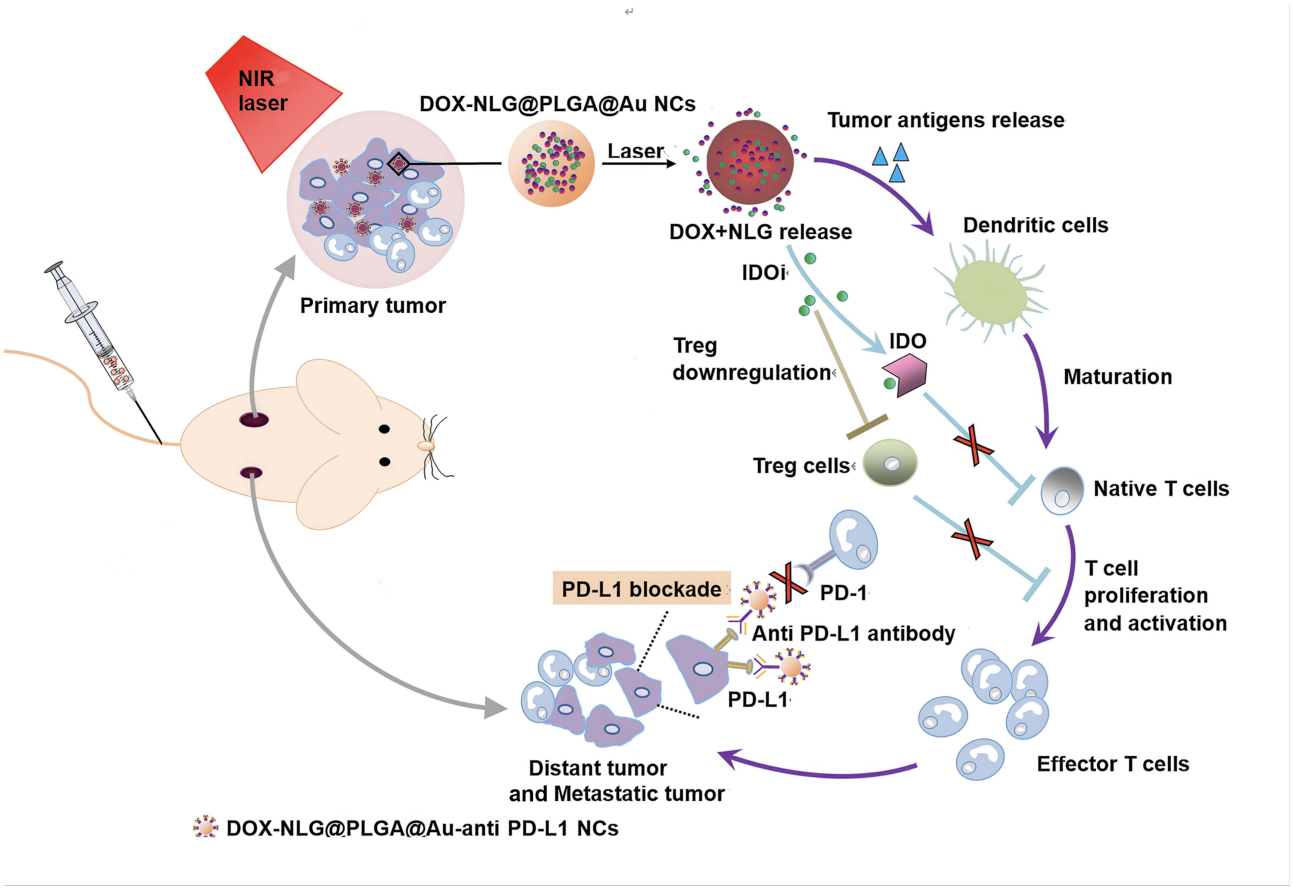

Figure 1 Schematic diagram of the antitumor mechanism of DNPA-aPD-L1 NCs. DOX-NLG@PLGA@Au-anti PD-L1 NCs, through active targeting and EPR effects, reach the tumor site, where they induce ICD via chemotherapy and photothermal therapy, synergistically inhibiting IDO and blocking PD-L1 to activate T cell immune programming and enhance sensitization therapy for primary TNBC lesions, thereby inhibiting the growth of metastatic tumors.

enhance tumor immunogenicity, inhibit IDO activity and relieve immunosuppression in the tumor microenvironment. Furthermore, the blocking of the PD-1/PD-L1 signaling pathway stimulates the body's antitumor immune response, resulting in a programmed synergistic sensitization therapy of the primary TNBC tumor to prevent tumor recurrence and metastasis. Moreover, it can facilitate photoacoustic molecular imaging, enabling the visualization and identification of TNBC. The designed DOX-NLG919@PLGA@Au-antiPD-L1 NCs (DNPA-aPD-L1 NCs) for in vivo chemotherapy and photothermal therapy induce ICD to synergistically inhibit IDO and block PD-L1 to activate T cell immunity for programmed sensitization therapy of TNBC primary lesions and inhibit the growth of metastatic tumors. The underlying mechanisms of these processes are delineated in Figure 1.

Materials and Methods

Materials

Navoximod (NLG919), dichloromethane (DCM), and polyvinyl alcohol (PVA, l788 low-viscosity type, alcohol solubility 87.0–89.0 mol/mol) were purchased from Aladdin Reagent Co., Ltd., Shanghai. 1-(3-dimethylaminopropyl)-3-ethylcarbamic acid hydrochloride (EDC), N-hydroxy-succinimide (NHS), poly(lactic-co-glycolic acid) (PLGA, 50:50, Mw 24,000–38,000) and polyacrylamide hydrochloride (PAH, Mw ~17,500) were purchased from Sigma-Aldrich Corporation (USA). sodium citrate, hydroxylamine hydrochloride (analytical grade) and sodium chloride (NaCl, > 99.8%) were purchased from Sinopharm Chemical Reagents Co., Ltd., sodium borohydride (Shanghai Runjie Reagents Co., Ltd). Trichloride gold acid ($HAuCl_4 \cdot 3H_2O$, Acros Corporation, USA), SH-PEG-COOH (Mw 2000, Shanghai Pengshuo Biotechnology Co., Ltd), FITC-labeled anti-PD-L1 antibody (Abcam Company, USA), DIR iodide

https://doi.org/10.2147/IJN.S539732

(Shanghai Fusheng Biotechnology Co., Ltd., China), doxorubicin hydrochloride (DOX) and D-luciferin potassium salt (98%) were purchased from Shanghai Meilun Biotechnology Co., Ltd.

Preparation of DNPA-aPD-L1 NCs

The DNPA-aPD-L1 NCs were prepared based on our previous method with modifications.[36] DOX-NLG919@PLGA nanoparticles (DNP NPs) were first synthesized using a single emulsion oil-in-water (O/W) solvent evaporation method. Briefly, PLGA (100 mg), DOX (10 mg), and NLG919 (20 mg) were dissolved in dichloromethane (5 mL) and emulsified at room temperature in PVA solution (2% w/v, 20 mL) using a syringe pump at a constant rate of 7.2 mL/h, followed by probe sonication (650 W, 4 s on/2 s off, 120 s). After solvent evaporation (24 h, 25°C), the nanoparticles were collected by centrifugation (10,000 ×g, 10 min) and washed three times with ultrapure water.

The gold nanoshell was formed according to a previous report.[27] The DNP NPs were coated with PAH (1 mg/mL in 0.5 M NaCl) to reverse their surface charge, enabling adsorption of citrate-stabilized AuNPs (~10 nm). Gold shell growth was initiated by adding hydroxylamine hydrochloride (0.33 mL, 0.5 M), yielding DOX-NLG919@PLGA@Au NCs (DNPA NCs).

For antibody conjugation, DNPA NCs (2 mg) were reacted with SH-PEG-COOH (5 mg, MW 2000 Da) in PBS for 24 h. After centrifugation and washing three times, FITC-labeled PD-L1 antibody was conjugated via EDC/NHS chemistry. The final DNPA-aPD-L1 NCs were purified and stored in PBS at 4°C.

Characterization of DNPA-aPD-L1 NCs

The morphology, elemental distribution, and size distribution of NCs were characterized by field emission scanning electron microscope (SEM, JSM-IT700HF, Japan), transmission electron microscopy (TEM, JEM1200EX, JEOL, Japan), energy-dispersive X-ray spectrometer (EDS, Bruker 6130, USA) and particle size analyzer (Malvern Instruments, Malvern, UK). The loading quantities of DOX and NLG919 in DNPA NCs were measured by HPLC (Sciex X500B QTOF, China). The distribution of gold in different tissues was measured by inductively coupled plasma emission spectrometer (ICP-MS, NexION5000G, USA). Laser scanning confocal fluorescence microscopy (LSCM, Olympus FV3000, Japan) was used to demonstrate the good binding of FITC-labeled antibodies with NCs.

Drug Loading and Encapsulation Efficiency

The drug loading (DL) and encapsulation efficiency (EE) of NLG919 and DOX within the NCs were quantitatively determined using high-performance liquid chromatography (HPLC). Standard solutions of NLG919 and DOX were prepared using 70% acetonitrile as the solution solvent. These standard solutions were analyzed using a Sciex X500B QTOF mass spectrometer. Characteristic peaks for each drug were identified based on their molecular weights, and the corresponding peak area-concentration data were recorded. Calibration curves were constructed by plotting the peak area (y-axis) against the concentration (x-axis) for each drug. To analyze the drug content, 100 μg of the nanocapsules was completely dissolved in 1 mL of 70% acetonitrile solution under vigorous vortexing to disrupt the PLGA matrix. The gold nanoshells were subsequently removed by centrifugation (12,000 rpm, 10 min). The supernatant was carefully collected and filtered through a 0.22 μm membrane prior to HPLC analysis. The concentration of each drug in the supernatant was calculated based on its respective calibration curve. The DL and EE were calculated using the following equations:

$$\mathrm{DL}(\%) = \frac{\text{Mass of drug encapsulated in NCs}}{\text{Total mass of NCs}} \times 100\%$$

$$\mathrm{EE}(\%) = \frac{\text{Mass of drug encapsulated in NCs}}{\text{Initial mass of drug}} \times 100\%$$

Drug Release Behavior Assessment

The drug release profiles of DNPA-aPD-L1 NCs under different pH conditions (pH 7.4 and 5.7) with near-infrared (NIR) laser irradiation were investigated. Specifically, 5 mg of DNPA-aPD-L1 NCs were dispersed in 2 mL of PBS buffer (pH 7.4 or 5.7) and placed in dialysis bags with a molecular weight cutoff of 5 kDa. Each bag was then immersed in a glass vial containing 20 mL of the corresponding PBS buffer and incubated in a constant temperature shaker at 37 °C. At predetermined time points (50, 110, and 170 min), 2 mL of the release medium was collected and replaced with an equal volume of fresh pre-warmed buffer. The concentrations of released DOX and NLG919 were determined by measuring the absorbance at 480 nm and 272 nm, respectively, using a UV-Vis spectrophotometer. To evaluate the NIR laser-triggered drug release, following each sampling time point, the system was irradiated with an 808 nm laser at a power density of 0.8 W/cm² for 10 min. After irradiation, an additional 2 mL aliquot was immediately collected for analysis and replaced with fresh buffer. This laser irradiation procedure was repeated for three cycles. The cumulative release of DOX and NLG919 from the NCs was calculated based on the measured drug concentrations.

Cell Experiments

Breast cancer cell lines 4T1 and 4T1-luc were purchased from the Chinese Academy of Sciences Cell Bank. These cells were cultured in RPMI-1640 medium supplemented with 10% fetal bovine serum (FBS) and 1% penicillin-streptomycin at 37°C and 5% humidity. Cells were passaged using trypsin-EDTA. All cells used in the experiment were in the logarithmic growth phase.

In vitro Targeting Ability Assessment

The targeted specific binding ability of DNPA-aPD-L1 NCs was detected by LSCM. 4T1 cells were seeded in LSCM-specific culture dishes (1×10^5/well) and incubated for 24 h. All cells were divided into three groups: target group (4T1 cells and FITC-labeled DNPA-aPD-L1 NCs), non-target group (4T1 cells and DNPA NCs), and competitive inhibition (blocked) group (4T1 cells pre-treated with aPD-L1 and DNPA-aPD-L1 NCs). NCs of the same concentration (100 μL, 100 μg/mL) were added to the corresponding culture medium, and the three groups of cells were incubated for 30 minutes. The cells were then fixed with 4% paraformaldehyde (10 minutes) and stained with DAPI (10 minutes). During this process, the cells were washed three times with physiological saline to remove unbound NCs and residual dye. Finally, the cellular uptake of DNPA-aPD-L1 NCs was observed using LSCM.

For flow cytometric quantification, 4T1 cells were seeded at a density of 1×10^6 cells/well in six-well plates and cultured for 24 hours. Beyond the experimental groups described above, two additional groups were included: a free fluorescently labeled antibody group (4T1 cells incubated with excess FITC-labeled aPD-L1 antibody) and a negative control group. Add 100 μL of NCs (100 μg/mL) or excess antibody to the corresponding culture medium, and then incubate for two hours. After cell digestion, obtain cell uptake data for each group using a BD FACS Celesta flow cytometer (BD Biosciences, USA).

Animal Model Establishment

We performed the animal studies according to the Guide for the Care and Use of Laboratory Animals published by US National Institutes of Health. All animal experiments were conducted in accordance with the approved protocol of the Institutional Animal Care and Use Committee (IACUC) of Renji Hospital Affiliated to Shanghai Jiao Tong University School of Medicine. Female Balb/c mice (6–8 weeks old, 18–22 g) were purchased from Hangzhou Ziyuan Laboratory Animal Co., Ltd. Establishment of a unilateral TNBC xenograft model: 4T1 cells (100 μL, 1×10^6) were suspended in 1× PBS solution and injected subcutaneously into the right axilla to establish a tumor model. Seven days later, tumors $\geq$70 mm^3 were considered positive for tumor. Tumor volume was monitored by measuring the longest diameter (length, L) and the perpendicular shorter diameter (width, W) using a digital caliper. The volume was calculated according to the following formula: $V = 1/2 \times L \times W^2$.

Visualization, Localization and Identification of TNBC Tissue

The ability of DNPA-aPD-L1 NCs to visualize and locate TNBC was validated by small animal photoacoustic imaging system (VEVO LAZR-X, FUJIFILM, Japan). Unilateral TNBC xenograft model mice were randomly divided into a targeted group and a non-targeted group, with four mice in each group. DNPA-aPD-L1 NCs and DNPA NCs (5 mg/mL, 250 μL) were administered via tail vein injection. Mice were anesthetized with isoflurane and fixed in the target region. Photoacoustic imaging was performed at different time points (pre-injection, 1 h, 2 h, 4 h, 6 h and 24 h) using small animal photoacoustic imaging system.

Tumor Targeting Ability, in vivo Distribution and Metabolism of DNPA-aPD-L1 NCs

Small Animal In Vivo Fluorescence Imaging System (IVIS Spectrum, PerkinElmer, USA) was used to monitor the imaging effects at tumor sites 2 h, 6 h, 24 h, 48 h, and 72 h after intravenous injection of DIR-labeled DNPA-aPD-L1 nanoparticles (200 μL, 5 mg/mL). The time at which fluorescence reached its peak at the target site was recorded. Unilateral TNBC xenograft model mice were randomly divided into a targeted group and a non-targeted group, with six mice in each group. Unmodified antibody DIR @PLGA@Au NCs served as the non-targeted group. To prevent the liver from interfering with fluorescence imaging at the tumor site, the tumor in this unilateral TNBC xenograft model was located on the left side. At different time points (48 h, 96 h, 168 h), the gold content in various organs, tissues, and metabolites (heart, liver, spleen, lungs, kidneys, blood, urine, feces, tumors) was measured using inductively coupled plasma mass spectrometry (ICP-MS). Animals are euthanized before organs removal. The gold content was converted to total dose percentage using the formula: $\%ID/g$ = measured concentration × organ weight/injection dose × 100%.

Photothermal Effect of DNPA-aPD-L1 NCs on TNBC

Unilateral TNBC xenograft model mice were randomly divided into five groups, with three mice per group. The treatment groups were administered the same dose (200 μL, 5 mg/mL) of DNPA-aPD-L1 NCs, DNPA NCs, DPA-aPD-L1 NCs, or PLGA@Au-aPD-L1 NCs (PA-aPD-L1 NCs) via tail vein injection, and the control group received 200 μL of physiological saline. Forty-eight hours after injection, infrared thermal imaging (Optris Infrared Sensing, Portsmouth, NH, USA) was used to image the temperature changes of the transplanted tumors in the treatment and control groups under near-infrared laser irradiation (808 nm, 0.8 W/cm²) for 5 minutes.

Synergistic Sensitization Effects of the Combined Therapy on Primary Tumors

Unilateral TNBC xenograft model were randomly divided into nine groups: DNPA-aPD-L1 NCs + laser group, DNPA NCs + laser group, DPA-aPD-L1 NCs + laser group, PA-aPD-L1 NCs (PA-aPD-L1 NCs, blank NCs) + laser group, saline + laser group, free DOX group (1.5 mg/kg), DNPA-aPD-L1 NCs group, DNPA NCs group and saline group, with 5 mice in each group. Each mouse received an injection of 200 μL (5 mg/mL) of the corresponding NCs or saline. The laser group received continuous laser irradiation (808 nm, 0.8 W/cm²) on the primary tumor site for 5 minutes, 48 hours after drug administration. Tumor growth curves were plotted to observe tumor recurrence. Additionally, 24 hours after treatment, one animal from each group was euthanized, and tumor tissue was resected for TUNEL and H&E staining analysis to further assess cell apoptosis and necrosis induced by different treatment methods. The survival rate and survival time of the remaining 4 mice in the same group were observed and recorded (with the day of drug injection as day 0), for a total of 40 days. To ensure ethical standards and animal welfare in animal experiments, mice were euthanized when the tumor volume exceeded 2000 mm³ or any dimension exceeded 20 mm.

Long-Term Inhibitory Effects of the Combined Therapy on Recurrent and Regenerated Tumors

Establishment of a TNBC recurrent and regenerated tumor model: Unilateral TNBC xenograft model in mice were treated with PPT or surgical resection, resulting in nearly complete tumor clearance with only 1% of tumor tissue remaining in the surgical resection area to mimic recurrent tumors. On day 3 post-treatment, 4T1 cells (1×10^6 cells/100 μL/mouse) were implanted into the left axillary region of the mice to simulate regenerative tumors. The tumor-

bearing mice were randomly divided into 9 groups, with 5 mice per group, and the experimental groups were the same as before. Each mouse was administered the same dose of NCs (200 μL, 5 mg/mL) or physiological saline via tail vein injection. Forty-eight hours after injection, the primary tumor site was irradiated with continuous laser waves (808 nm, 0.8 W/cm²) for 5 minutes. The tumors were observed for 15 days and their volumes were measured. The in situ recurrence rates, survival rates and volumes of regenerated tumors were compared among the different treatment groups.

Combined Therapy Achieves Synergistic Sensitization and Targeted Treatment of Primary and Metastatic Tumors

Establishment of primary tumor and metastatic tumor mouse models: inoculate 4T1 cells (1×10^6 cells/100 μL/mouse) subcutaneously into the right axillary region of mice as the primary tumor. Three days later, inoculate the same number of 4T1 cells into the contralateral axillary region of mice as the metastatic tumor. On day 5 post-treatment, circulating tumor cells were administered via tail vein injection using 4T1-Luc cells (1×10^5 cells/100 μL/mouse). The tumor-bearing mice were randomly divided into 9 groups with the same experimental grouping as before, 6 mice per group. Each mouse was injected with the same dose of NCs or saline (200 μL, 5 mg/mL) via the tail vein. Forty-eight hours after injection, the primary tumor site was irradiated with continuous laser waves (808 nm, 0.8 W/cm²) for 5 minutes. The size of the primary tumor and distant metastatic tumors were measured every 3 days, and their volumes were calculated. Observations were continued for 15 days, and growth curves were plotted and observed for primary tumor recurrence and distant metastatic tumors. The survival rates of tumor-bearing mice in different treatment groups were compared. On days 10 and 20 after injection of 4T1-luc cells, mice were injected with a bioluminescence-related substrate, and fluorescence imaging of lung tissue was performed. After the last imaging session, the mice were euthanized, and the number of lung metastatic lesions was counted.

Effects of Photochemotherapy on Activating Non-Specific Immune Functions

To investigate whether NCs promote the expression of heat shock protein 70 (HSP70) in tumor tissues and induce changes in cytokine levels in immune organs, we randomly divided TNBC mice into 9 groups, with 6 mice per group, following the same grouping as in the previous experiment. Twenty-four hours after the corresponding drugs were administered via tail vein injection in mice, three tumor-bearing mice were randomly selected from each group for euthanasia. Subcutaneous tumors and spleens were excised, and the expression of HSP70 in breast cancer tumors was detected using immunohistochemistry. ELISA kits were used to detect the levels of cytokines, including IFN-γ, IL-2, IL-12 and TNF-α in the spleen tissue of 3 tumor-bearing mice from each group on day 7 of treatment.

Effects of Combined Sensitization Therapy on Inducing Tumor ICD

To verify whether combined therapy can enhance the immunogenicity of dead tumor cells and induce an antitumor immune response, TNBC mice were randomly divided into 9 groups, with 3 mice in each group, with the same experimental grouping as above. 24 hours after treatment, tumor-bearing mice were euthanized, and complete tumor tissues were collected for Western blot analysis of calmodulin (CRT) and high-mobility group box 1 (HMGB1) expression at the tumor site. Image J software was used for quantitative analysis of the bands.

In vivo Toxicity Experiment

Twelve healthy female Balb/c mice aged 6–8 weeks were selected as animal models to study the in vivo toxicity of DNPA-aPD-L1 NCs. DNPA-aPD-L1 NCs (250 μL, 5 mg/mL) were administered via tail vein injection. Three mice were sacrificed at 4 h, 12 h, 24 h and 72 h post-injection, and tissues (heart, liver, spleen, lung, kidney) and blood samples were collected for further analysis. Additionally, three mice were selected as the control group, which received PBS injections (0.3 mL per injection). Serum biochemical analysis was performed to quantitatively evaluate two important liver function indicators (alanine transaminase [ALT] and aspartate transaminase [AST]), one cardiac function indicator (creatine kinase MB isoenzyme [CK-MB]), and two renal function indicators (serum creatinine [CREA] and blood urea nitrogen [BUN]).

Statistical Analysis

The data were represented as mean ± SD. The comparisons of the mean value were performed by two-tailed Student's *t*-test. Statistical significance was defined as * $P < 0.05$, ** $P < 0.01$, *** $P < 0.001$, **** $P < 0.0001$. Western blot images were obtained, and signal intensities were calculated using Image J software.

Results

Characterization of NCs

NCs were synthesized using the water-in-oil single emulsion solvent evaporation method. The prepared DNPA-aPD-L1 NCs were black solutions with good water solubility, an average particle size of 258.9 ± 101.9 nm (Figure 2A), and a Zeta potential of −25.5 ± 7.04 mV (Figure 2B), meeting the general requirements for nanoparticle size in acoustic imaging agents. As shown in the TEM image (Figure 2C), the uncoated PLGA nanoparticles (DNP NPs) exhibited a smooth surface and spherical morphology. In contrast, TEM imaging of the gold-coated NCs (Figure 2D) clearly revealed that gold nanoparticles were uniformly distributed on the surface of the PLGA polymer, forming a slightly rough and discontinuous shell with visible nanogaps between adjacent gold nanoparticles, while maintaining uniform particle size and good dispersion. SEM observations further confirmed the spherical morphology and good dispersion of the NCs (Figure 2E). The elemental distribution map of DNPA NCs (Figure 3A) shows that the main component of the nano-microcapsules is gold, accounting for 15.93%, with AI at 73.19% (Figure 3B and C). Since the carrier material for preparing the SEM samples was tin foil, whose main element is AI, a high percentage of AI was observed; carbon and oxygen content were 10.17% and 0.71%, respectively. Since NCs contain PLGA, whose molecular formula is $(C_3H_4O_2)n$

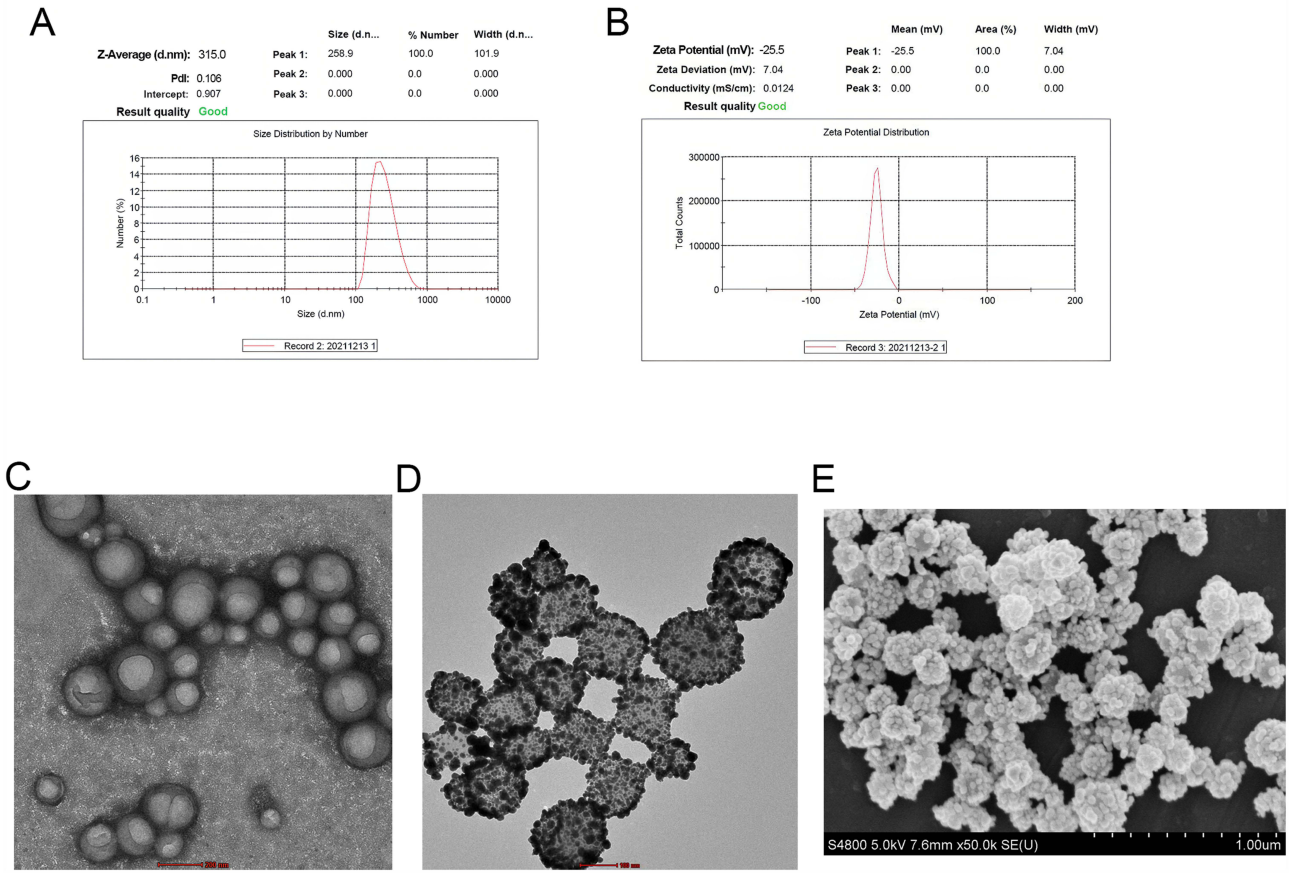

Figure 2 Manufacture and characterization of NCs. (**A**) Average particle size of DNPA NCs. (**B**) Zeta potential of DNPA NCs. The green text "Good" indicates that the uniformity and dispersion of the NCs solution are of good quality and meet the instrument output standards. (**C**) TEM image of NCs without gold nanocapsule shells. Scale bar, 200 nm. (**D**) TEM image of DNPA NCs. Scale bar, 100 nm. (**E**) SEM image of DNPA NCs. Scale bar, 1 μm.

 https://doi.org/10.2147/IJN.S539732

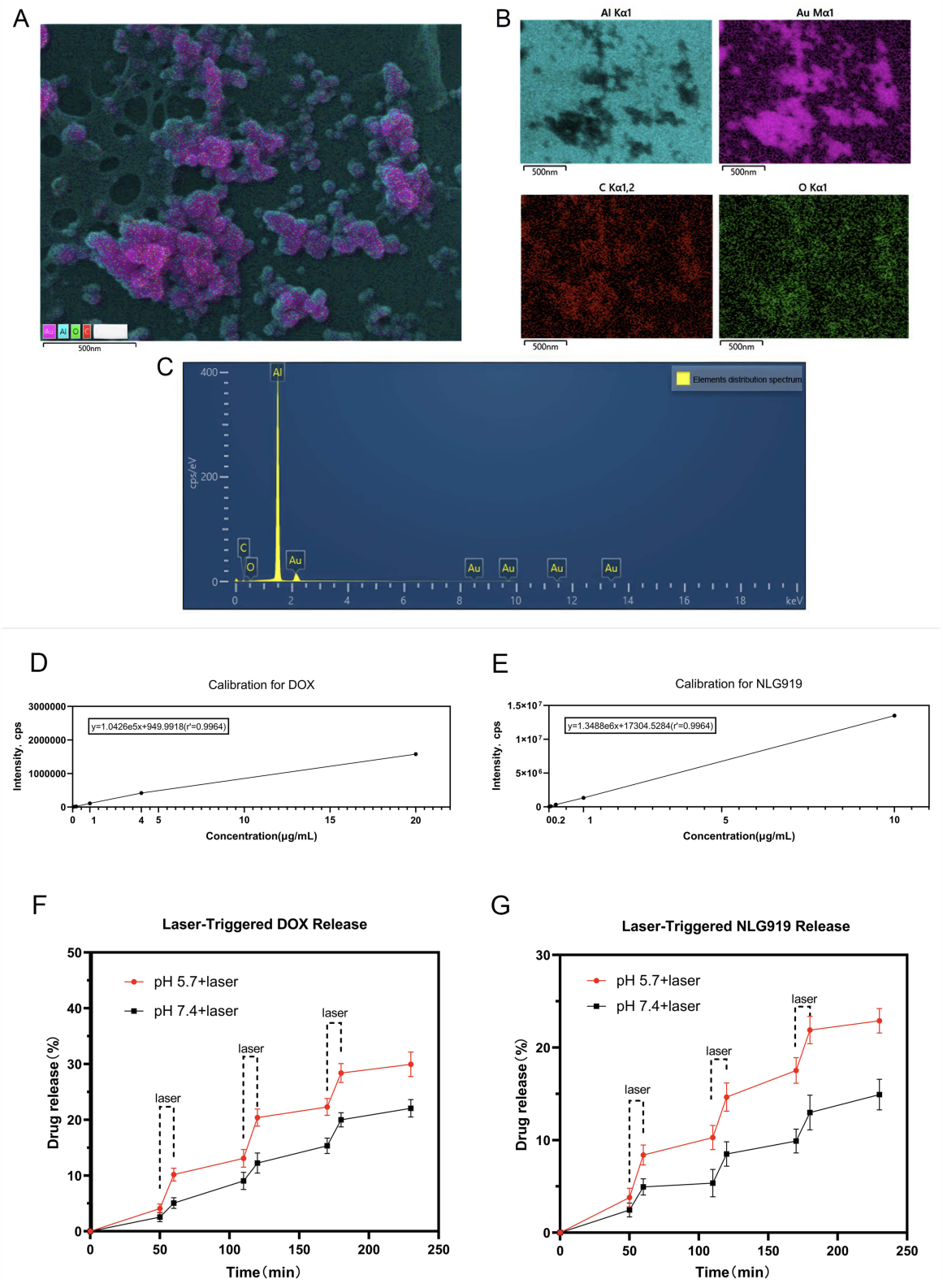

Figure 3 Elemental analysis of NCs. (**A**) Distribution of gold elements in NCs. Scale bar, 500 nm. (**B**) Distribution of different elements in NCs. Scale bar, 500 nm. (**C**) Element distribution spectrum of NCs. (**D** and **E**) Calibration curves for DOX and NLG919 concentration and signal Intensity. (**F** and **G**) Drug release curves for DOX and NLG919.

https://doi.org/10.2147/IJN.S539732

$(C_2H_2O_2)$m, this is the reason why carbon and oxygen elements were detected. Elemental analysis confirmed high gold content in the NCs. A linear calibration curve was established between drug concentration and signal intensity (Figure 3D and E). The final calculations revealed drug loading efficiencies of 5.22 ± 0.19% for DOX and 7.78 ± 0.54% for NLG919 within the NCs, with encapsulation efficiencies of 42.17 ± 2.40% and 31.48 ± 3.40%, respectively.

Drug Release Behavior Assessment

In the laser-triggered drug release experiment, the DNPA-aPD-L1 NCs solution was irradiated with an 808 nm laser (0.8 W/cm², 10 min) at three time points: 50, 110, and 170 min. The temperature of the solution rapidly increased, promoting the decomposition of PLGA and further accelerating the release of DOX and NLG919. As shown in Figure 3F and G, drug release significantly increased after laser irradiation and slowed after the laser was turned off.

In a weakly acidic environment at pH 5.7, the cumulative release rates of DOX and NLG919 reached 28% and 22%, respectively, after three laser irradiation cycles, which were significantly higher than the corresponding release rates of 20% and 13% observed at pH 7.4 under the same laser conditions ($p < 0.05$). The enhanced drug release under laser irradiation may be attributed to the photothermal effect of the gold nanoshells, which induced the degradation of the PLGA matrix and disrupted its structure, allowing the encapsulated drugs to be released through gaps in the gold nanoshell. These findings lay a foundation for further research into combined chemotherapy and photothermal therapy using targeted nanomaterials.

In vitro Targeting Ability Assessment

As shown in the dashed box in Figure 4, under LSCM, green fluorescence was observed in NCs, indicating that the FITC-labeled PD-L1 antibody has successfully bound to the surface of NCs. Meanwhile, red fluorescence indicated that DOX has been successfully encapsulated. The in vitro targeting performance was tested using PD-L1-highly expressing 4T1 cells. We observed that 4T1 cells (blue fluorescence) were extensively surrounded by FITC-labeled (green fluorescence) targeted NCs, while no significant fluorescence aggregation was observed on the surface of cells in other groups. This confirmed the targeting ability of PD-L1-targeted NCs toward 4T1 cells. Flow cytometry results were consistent with laser confocal imaging (Figure 5A), showing that the binding rate of DNPA-aPD-L1 NCs in the target group to 4T1 cells was significantly higher than that in the control group, non-target group, and competitive inhibition (blocked) group. We also observed that the cell binding rates of targeted group and free fluorescently labeled antibody group were comparable, at 67.2 ± 1.5% and 56.5 ± 2.5%, respectively. These two experimental results further demonstrate that the antibody was successfully conjugated to NCs surface and retained full functionality.

Visualization, Localization, and Identification of TNBC Tissue

To validate the ability of multifunctional targeted NCs to visualize and localize TNBC, we performed PAI experiments. As shown in Figure 5B, after injection of the targeted group NCs, the photoacoustic imaging signals in the tumor tissue gradually increased over time, reaching the highest levels at 24 h with the best imaging quality, and the photoacoustic imaging signals basically covered the entire tumor tissue area. However, the non-targeted group showed only sparse photoacoustic signals within the tumor tissue. Quantitative analysis results also demonstrated (Figure 5C) that at 6 h and 24 h, the photoacoustic signal intensity in the targeted group was significantly higher than that in the non-targeted group.

Tumor Targeting Ability, in vivo Distribution and Metabolism of DNPA-aPD-L1 NCs

To more accurately validate the systemic distribution of NCs in vivo, the time to reach peak accumulation at the tumor site, the drug retention time at the target site and the imaging effects, DIR-labeled DNPA-aPD-L1 NCs and DNPA NCs were intravenously injected into tumor-bearing mice. As shown in Figure 5D, with time, red fluorescence gradually accumulated and increased in the tumor tissue of the targeted group, reaching a peak at 48 h with the strongest fluorescence intensity, followed by a gradual decline. In contrast, no significant fluorescence aggregation was observed in the tumor tissues of the non-targeted group, indicating that the drug-loaded targeted NCs we prepared can target and aggregate in TNBC tumor regions. Fluorescence aggregation was also observed in the liver of both groups. The results of gold element distribution in vivo measured by ICP-MS (Figure 5E) were consistent with the above findings, with the

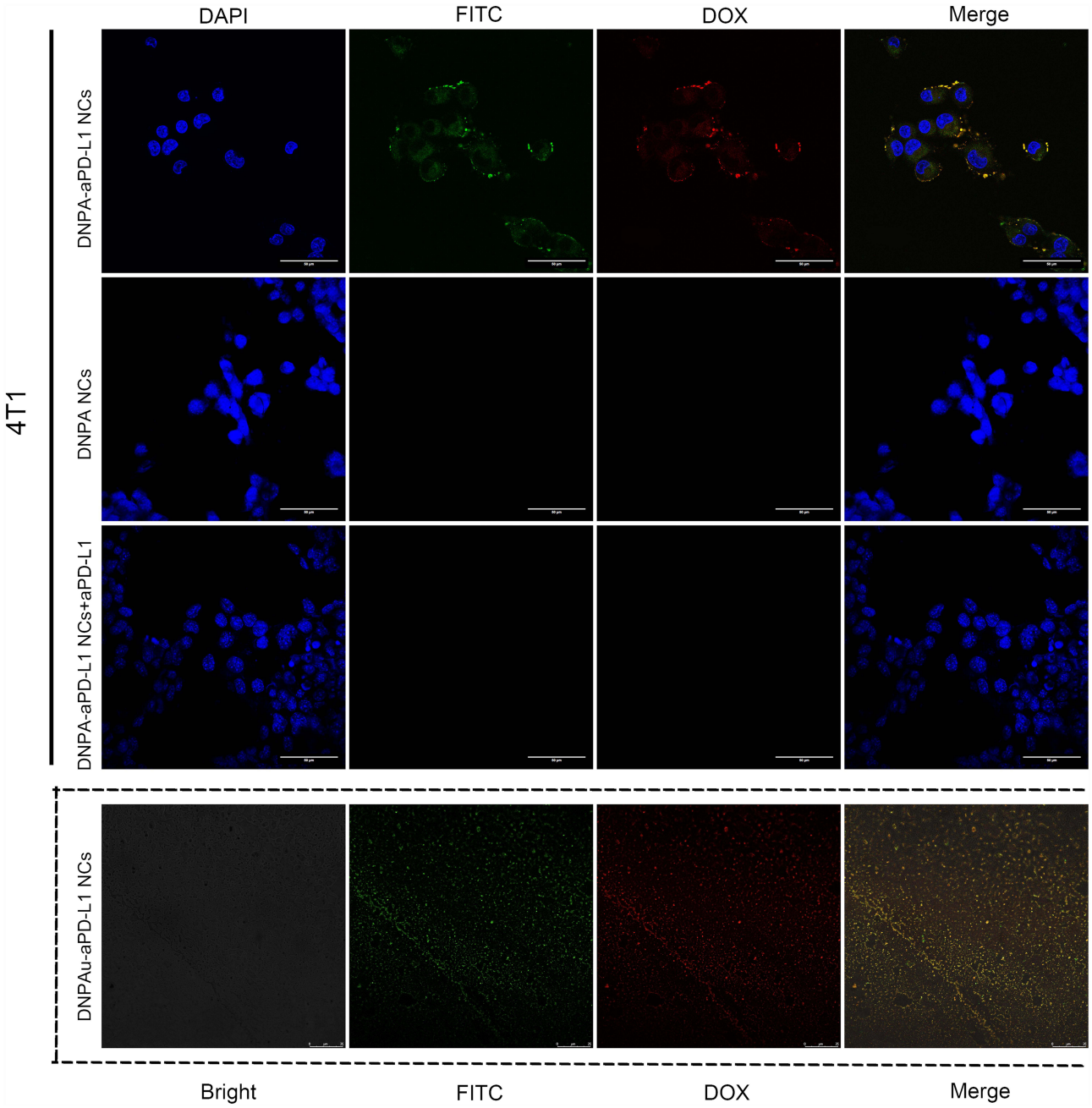

Figure 4 In vitro targeting ability of NCs. 4T1 cells incubated with DNPA-aPD-L1 NCs (1st row), DNPA NCs (2ND row) and 4T1 cells pre-treated with aPD-L1 blockade co-incubated with DNPA-aPD-L1 NCs (3RD row), Scale bar: 50 μm. Confocal laser scanning microscopy images of DNPA-aPD-L1 NCs showing antibody conjugation and drug loading (dashed box), scale bar: 25 μm.

highest accumulation of gold elements in the liver and kidneys at 96 h, with some accumulation in the spleen, confirming that NCs are primarily metabolized via the liver and kidneys. Additionally, the gold content in the body gradually decreased seven days post-injection, with metabolites consistently containing a certain amount of gold, indicating that gold NCs can be metabolized and excreted from the body within a short period. The results of fluorescent in vivo imaging studies in small animals indicate that the PD-L1 receptor can serve as an important molecular target for locating and recognizing breast cancer-targeted drug-loaded NCs. The targeted NCs we prepared can specifically accumulate in the target area, aiding in the realization of targeted, visualizable molecular imaging for TNBC.

https://doi.org/10.2147/IJN.S539732

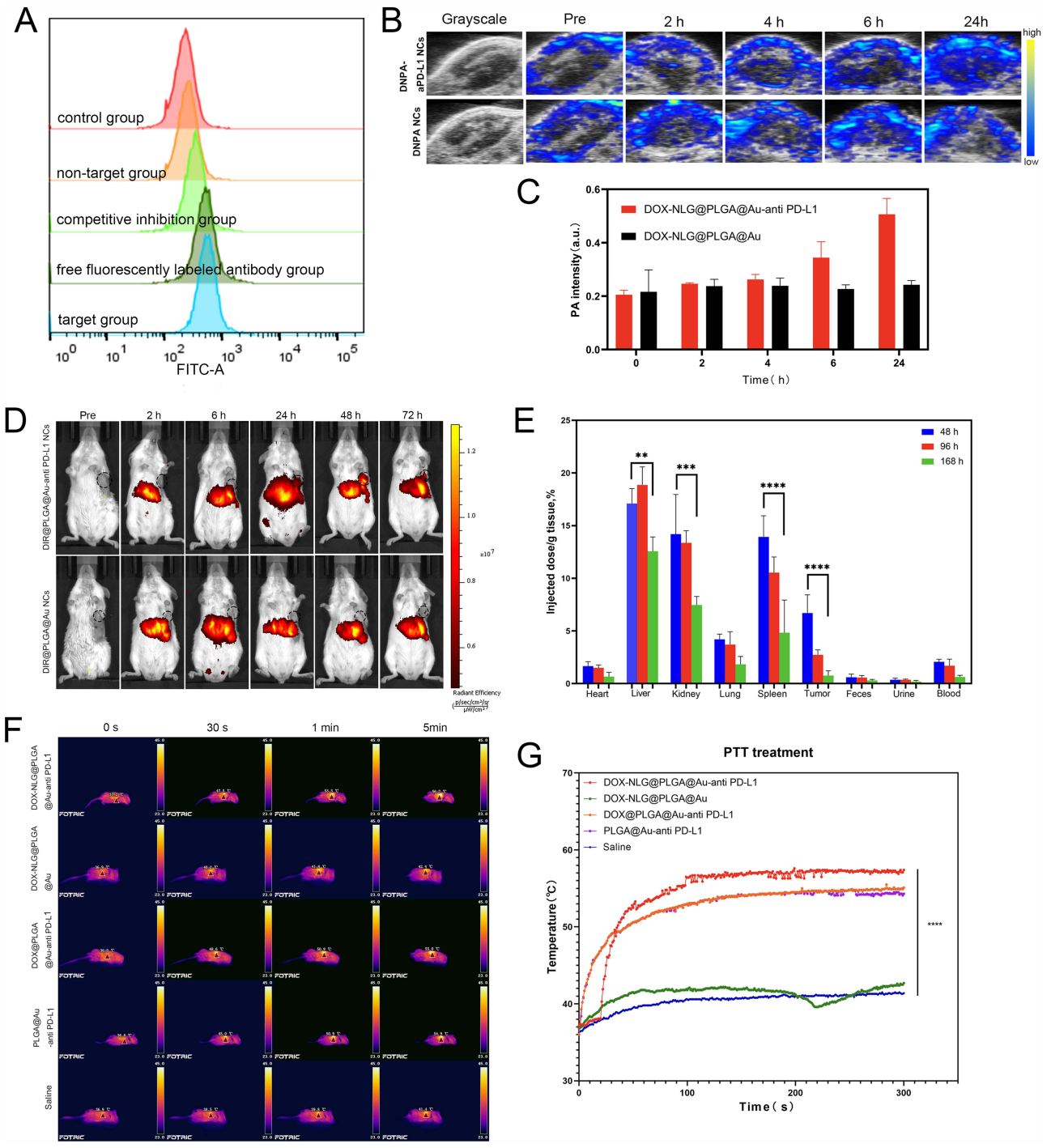

Figure 5 Evaluating the targeting and imaging capabilities of NCs. (**A**) Flow cytometry assessment of NCs targeted binding efficiency. (**B**) In vivo PAI of NCs. (**C**) Quantitative analysis of in vivo PAI columnar diagram. (**D**) In vivo fluorescence imaging of NCs. (**E**) Detection of gold content in different tissues using ICP-MS. (**F**) Photothermal effects of NCs in vivo. (**G**) Time-temperature curve of photothermal effects in vivo. The results are the mean ± SEM.** represents $P < 0.01$, *** represents $P < 0.001$ and **** represents $P < 0.0001$.

Photothermal Effect of DNPA-aPD-L1 NCs on TNBC

To verify the excellent photothermal conversion capability of multifunctional targeted NCs and their ability to guide near-infrared laser irradiation for tumor photothermal therapy in vivo, we conducted photothermal imaging experiments. As shown in Figure 5F and G, the temperature changes at the tumor site in the targeted treatment group mice can be observed. As the irradiation time increases, the tumor site gradually becomes brighter orange, indicating three targeted

groups: DNPA-aPD-L1 NCs, DPA-aPD-L1 NCs and PA-aPD-L1 NCs rapidly increased within 5 minutes, reaching temperatures above 54°C, sufficient to kill the transplanted tumor cells. In contrast, the non-targeted group mice, which received saline or DNPA NCs, exhibited a darker orange-yellow color at the transplanted tumor site after laser irradiation, with temperatures only rising to 40–42°C. This experiment demonstrates that DNPA-aPD-L1 NCs have excellent photothermal therapy potential in vivo.

Synergistic Sensitization Effects of the Combined Therapy on Primary Tumors

To validate the synergistic sensitization efficacy of DNPA-aPD-L1 NCs combined with laser therapy on TNBC, we selected the time point 48 h after intravenous injection for irradiation based on in vivo fluorescence imaging results. The modeling and treatment process is shown in Figure 6A. As shown in Figure 6B and C, compared with the control group, the tumor tissue at the irradiation site in the targeted laser group (DNPA-aPD-L1 NCs + laser, DPA-aPD-L1 NCs + laser, PA-aPD-L1 NCs + laser) exhibited significant apoptosis and necrosis within seven days, with tumor growth significantly inhibited and nearly completely disappeared by day 3. Among these, the tumors in the first group (DNPA-aPD-L1 NCs + laser) of mice exhibited the most pronounced inhibition, while tumor growth in the free DOX group was only mildly

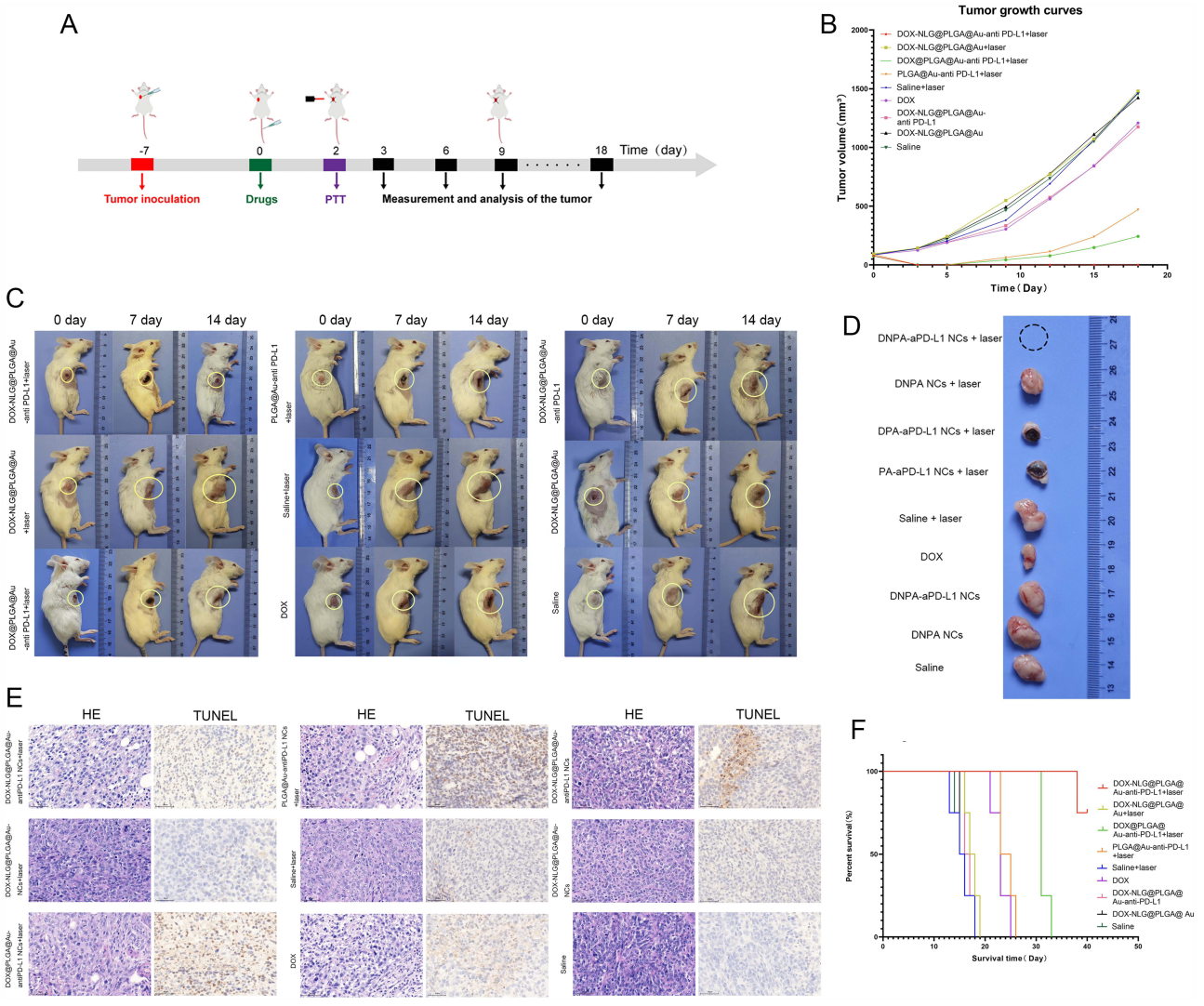

Figure 6 Treatment of Unilateral TNBC xenograft model. (**A**) Flowchart of Unilateral TNBC xenograft modeling and experimental process. (**B**) Growth curve of the primary tumor. (**C** and **D**) Representative photos of TNBC in situ tumor model mice and tumors at days 0, 7, and 14 during treatment. (**E**) H&E and TUNEL images of tumor tissues 24 h post-treatment (×400 magnification). (**F**) Survival time and survival rate of mice in different groups.

https://doi.org/10.2147/IJN.S539732

inhibited, and no significant inhibition was observed in the non-targeted group and the non-laser group. As shown in Figure 6D, tumor specimens from the primary transplanted tumors were extracted on day 7 post-treatment: mice in the DNPA-aPD-L1 NCs + laser group showed no visible tumor tissue after treatment, while mice in the other two groups (DPA-aPD-L1 NCs + laser, PA-aPD-L1 NCs + laser) exhibited extensive necrosis in the tumor regions and mice in the DOX alone group showed only mild inhibition of tumor size. From days 8 to 10 post-treatment, no measurable tumors were observed at the primary tumor sites in the DNPA-aPD-L1 NCs + laser group, and no significant tumor recurrence was observed over the subsequent 20-day observation period. In contrast, tumors in the other targeted NCs with or without drug + laser groups showed a tendency toward recurrence, while tumor growth trends in the free DOX group, non-targeted group, and non-laser group were not significantly different from the control group. HE and TUNEL staining results indicated that tumor tissues were significantly disrupted in the three targeted laser groups post-treatment, with an increased number of apoptotic tumor cells (Figure 6E). Follow-up observations up to 40 days (Figure 6F) showed that some mice in the DNPA-aPD-L1 NCs + laser group remained alive, with a survival rate of 75%, while all mice in the other groups died. In summary, the combined therapy of DNPA-aPD-L1 NCs + laser demonstrated the best therapeutic effect, with tumor recurrence inhibition and significantly prolonged the survival of TNBC mice.

Long-Term Inhibitory Effects of the Combined Therapy on Recurrent and Regenerated Tumors

The high recurrence rate of TNBC is one of the major challenges in treating this disease. To validate the efficacy of our treatment strategy in inhibiting tumor recurrence and regeneration in vivo, as shown in Figure 7A, we established a mouse model of TNBC recurrence and regenerative tumors. As shown in Figure 7B–D, in the targeted drug + laser group (DNPA-aPD-L1 NCs + laser, DPA-aPD-L1 NCs + laser), no recurrent tumors were observed at the primary tumor site after treatment, with visible healing scars. In the NLG919 drug-containing laser group, no obvious regenerated tumors were observed on the contralateral side over 15 days of continuous observation. The group without NLG919 drug + laser showed slow growth of regenerated tumors on the contralateral side. The PA-aPD-L1 NCs + laser group without drugs in NCs not only showed a tendency for recurrence at the primary site but also uninhibited growth of regenerated tumors on the contralateral side. The free DOX group, although it could partially inhibit tumor recurrence, failed to suppress tumor regeneration. In other groups, after surgical treatment, the primary tumor site showed mild elevation at the suture margins, indicating a tendency for recurrence, and the contralateral regenerated tumors exhibited growth trends approaching those of the control group. Our study results indicate that targeted NCs loading DOX-NLG combined with laser irradiation can prevent the recurrence of primary transplanted TNBC tumors and effectively inhibit the growth of regenerated tumors. This suggests that the photothermal effects of laser irradiation, the light-controlled release of chemotherapy drug DOX, and the immune checkpoint PD-L1 blockade combined with NLG-mediated IDO inhibition exert a synergistic and programmed effect in preventing tumor recurrence and regeneration.

Combined Therapy Achieves Synergistic Sensitization and Targeted Treatment of Primary and Metastatic Tumors

TNBC is highly invasive and prone to distant metastasis, with the lungs being the most common site of metastasis. Therefore, we established TNBC primary, distant metastatic tumors, and lung metastasis models (Figure 8A) and all treatment groups were shown in Figure 8B. As shown in Figure 8C and D, the combination of targeted NCs loading drugs and laser therapy achieved the best therapeutic effects, with significant apoptosis and necrosis of the primary tumor and marked inhibition of metastasis growth. Among these, the group treated with NCs loaded with NLG919 and DOX combined with laser irradiation exhibited the most significant tumor growth inhibition. After continuous observation of the mice in each group for 40 days, as shown in Figure 8E, the survival rate was highest in the DNPA-aPD-L1 NCs combined with laser therapy group, with a survival rate of 75% on day 34 and 25% on day 40. The average survival time was significantly longer than that of other groups, reaching 36 days. In contrast, the group treated with DOX-loaded targeted NCs plus laser irradiation showed a higher survival rate, with an average survival time of 23 days, while the average survival time in the other seven groups did not exceed 20 days, and most mice died around day 15. As shown in Figure 8F and G, by day 10, lung metastasis foci were

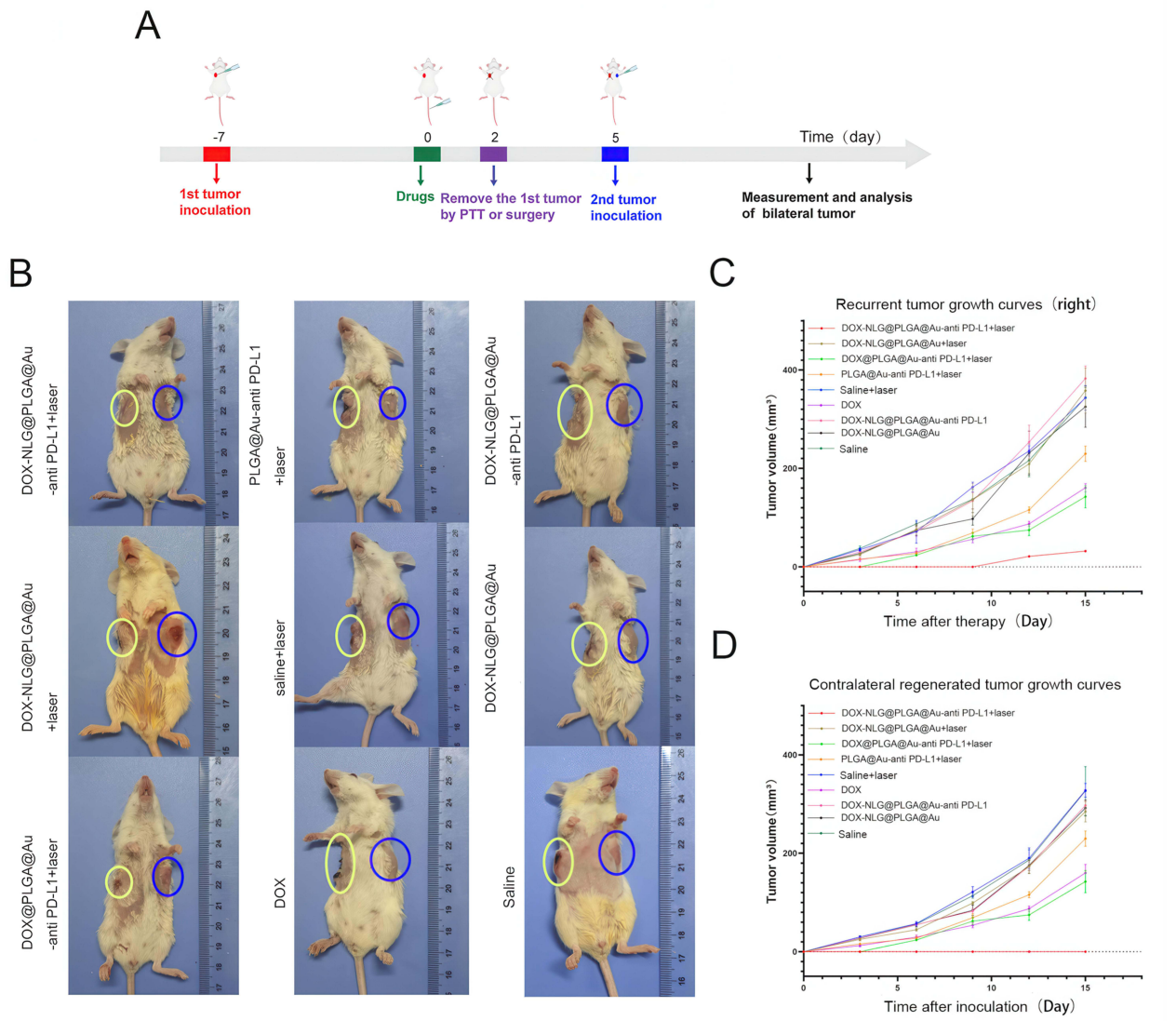

Figure 7 Treatment of TNBC primary tumors and regenerated tumors. (**A**) Flowchart of TNBC primary tumors and regenerated tumors modeling and experimental process. (**B**) Representative photographs of mice 7 days after inoculation of contralateral regenerated tumors (yellow circles indicate the locations of primary and recurrent tumors, blue circles indicate regenerated tumors). (**C** and **D**) Tumor growth curves of recurrent tumors and contralateral regenerated tumors.

observed in all groups except the DNPA-aPD-L1 NCs + laser group. On day 20, all groups of mice were examined. The DNPA-aPD-L1 NCs + laser group still showed no obvious metastatic lesions, while the remaining mice in other groups exhibited significant pulmonary metastasis, which was more widespread compared to day 10. Notably, some mice developed extensive bone metastatic lesions in the thighs and pelvic regions. Macroscopic specimens of lung metastatic tumors (Figure 8H) were consistent with the in vivo fluorescent imaging of the lungs, no obvious metastatic lesions were observed in the first group throughout the study. Based on the above experimental results, it is demonstrated that DNPA-aPD-L1 targeted NCs prepared by our group, after laser irradiation, not only exhibit significant antitumor therapeutic effects in the laser-irradiated region but also significantly inhibit metastatic tumors, thereby reducing the risk of distant lung metastasis and significantly prolonging the survival of tumor-bearing mice.

Effects of Photochemotherapy on Activating Non-Specific Immune Functions

To further explore the impact of the antitumor effects triggered by our prepared NCs after photochemotherapy on the activation of the body's non-specific immune response, the expression levels of HSP70 in tumor tissues and changes in

https://doi.org/10.2147/IJN.S539732

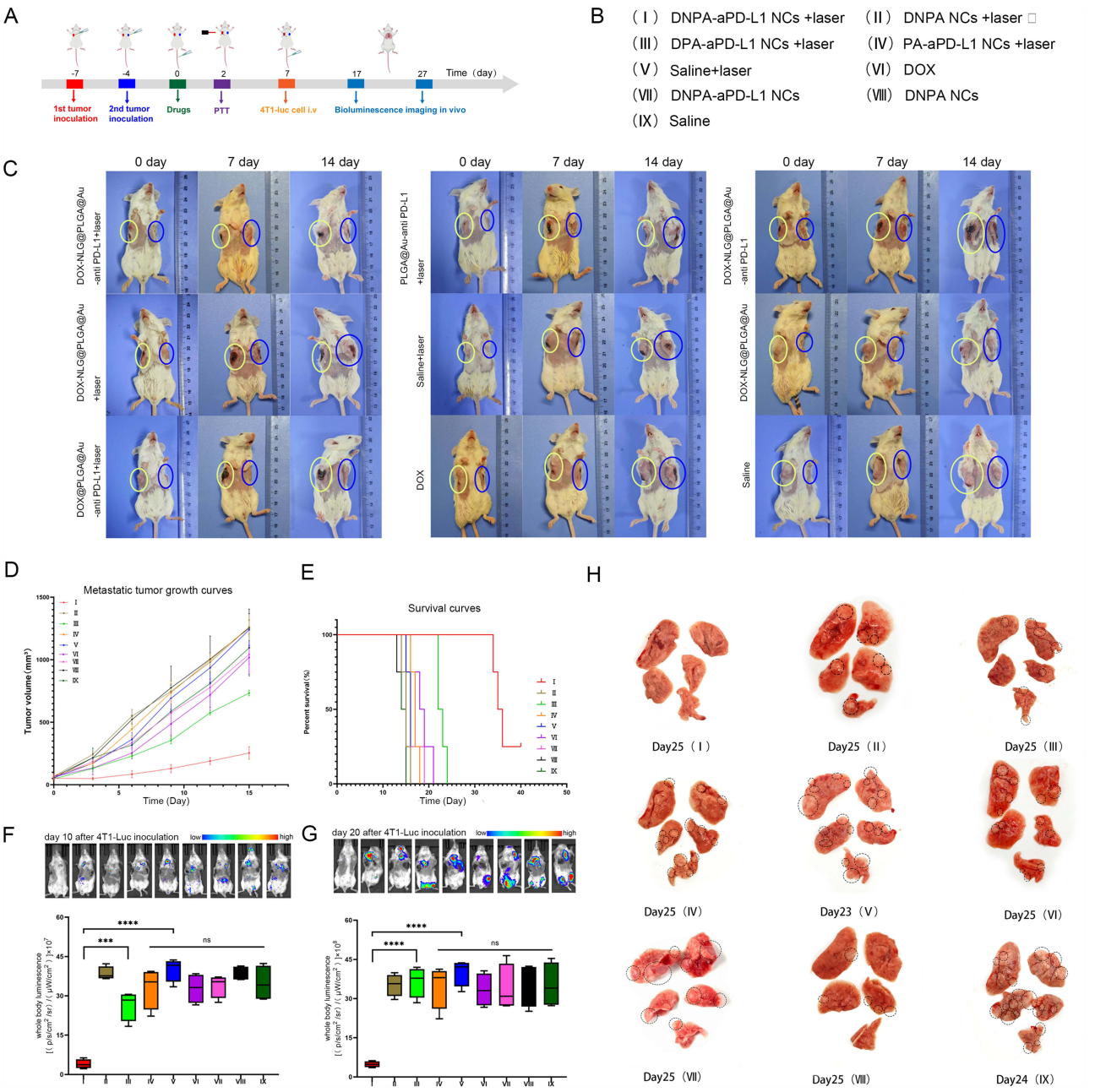

Figure 8 Treatment of TNBC primary tumors and metastatic tumors. (**A**) Flowchart of the modeling and experimental process of TNBC primary tumors and metastatic tumors. (**B**) Treatment schedule for mice received. (**C**) Representative photographs of mice on days 0, 7, and 14 during treatment (yellow circles indicate the locations of primary tumors, blue circles indicate metastatic tumors). (**D** and **E**) Metastatic tumor growth curves, survival time, and survival rates of mice in each group. (**F** and **G**) In vivo fluorescence imaging of mice 10 days and 20 days after tail vein injection of 4T1-luc cells. The results are the mean ± SEM (n = 6). ns represents no statistically significant difference. *** represents $P < 0.001$, and **** represents $P < 0.0001$. (**H**) Representative photographs of lung metastatic lesions in mice from each group (dotted circles indicate visible lung metastatic lesions).

cytokines in the spleen were detected. The expression of HSP70 protein in tumor tissues of different treatment groups were shown in Figure 9A. After quantitative analysis using Image J software (Figure 9B), the HSP70 protein content in the targeted drug + laser group and the free DOX group was significantly different from that in the control group and the non-laser treated group. Furthermore, as shown in Figure 9C, ELISA kits were used to detect spleen tissue in each group. The levels of IFN-γ, IL-2, IL-12 and TNF-α in the spleen of the targeted NCs + laser group were significantly higher than those in the control group. This indicates that the targeted drug-loaded NCs we prepared exhibit significant non-specific immune-enhancing effects after laser trigger.

https://doi.org/10.2147/IJN.S539732

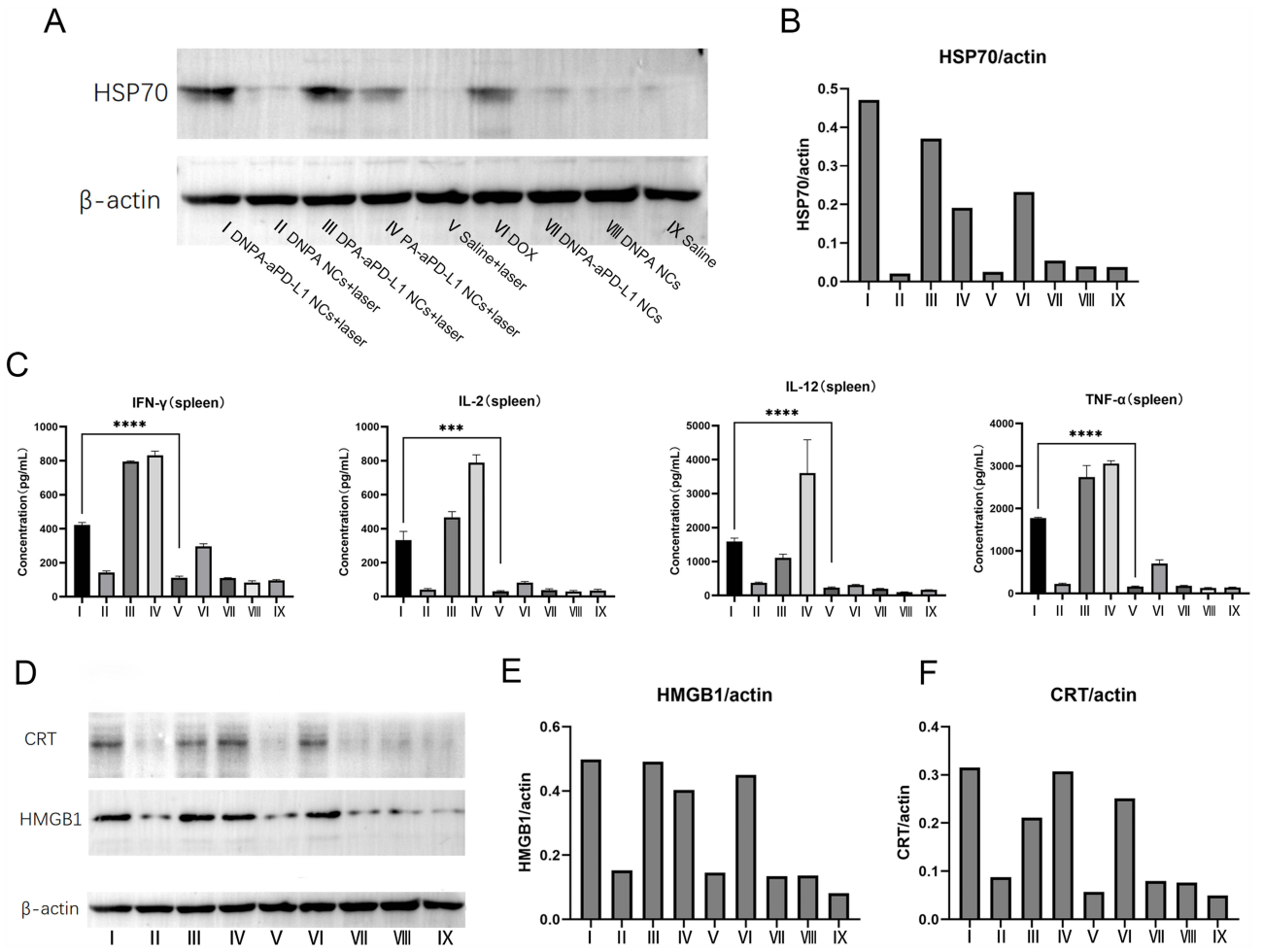

Figure 9 The mechanism of NCs activating the body's non-specific immune response. (**A**) Expression of HSP70 protein in tumors of mice in each group was analyzed by Western blot. (**B**) Quantitative analysis of HSP70 protein expression levels. (**C**) Cytokine levels (IFN-γ, IL-2, IL-12 and TNF-α) in spleen cells of mice from each group on day 5 post-treatment. (**D**) Expression of CRT and HMGB1 proteins in tumors of mice in each group was analyzed by Western blot. (**E** and **F**) Quantitative analysis of CRT and HMGB1 protein expression levels. *** represents $P < 0.001$, and **** represents $P < 0.0001$. Shared β-actin loading control for HSP70/CRT/HMGB1 validated by: (1) Identical tissue aliquots,(2) Synchronized multi-membrane processing,(3) Technical verification: Inter-membrane CV=3.94% (n=6), linear dynamic range R^2=0.996.

Effects of Combined Sensitization Therapy on Inducing Tumor ICD

To verify whether combined therapy can enhance the immunogenicity of dead tumor cells and induce antitumor immune responses, Western blot analysis and Image J software quantification (Figure 9D–F) showed that the CRT protein and HMGB1 levels protein in the targeted NCs + laser group and the free DOX group were significantly higher than those in the control group. The elevation of CRT and HMGB1 after tumor treatment is a key event in the immunogenic cell death process induced by chemotherapy, photothermal therapy or radiotherapy. It enhances the immunogenicity of tumor cells, aiding the body in forming an effective antitumor immune response. This may be one of the immune mechanisms underlying the significant therapeutic effects of drug-loaded targeted NCs followed by laser irradiation on both primary and metastatic tumors in TNBC, reducing the risk of distant lung metastasis and significantly prolonging the survival of tumor-bearing mice.

In vivo Toxicity Experiment

During the experiment, no obvious signs of toxicity were observed in the experimental group. Blood biochemical analyses reflecting major organ function were conducted at different post-injection time points for all mice. As shown in Figure 10A–C, all biochemical parameters in mice treated with targeted NCs were within the range similar to those in mice treated with PBS. Figure 10D shows that no obvious histopathological abnormalities or tissue damage were

https://doi.org/10.2147/IJN.S539732

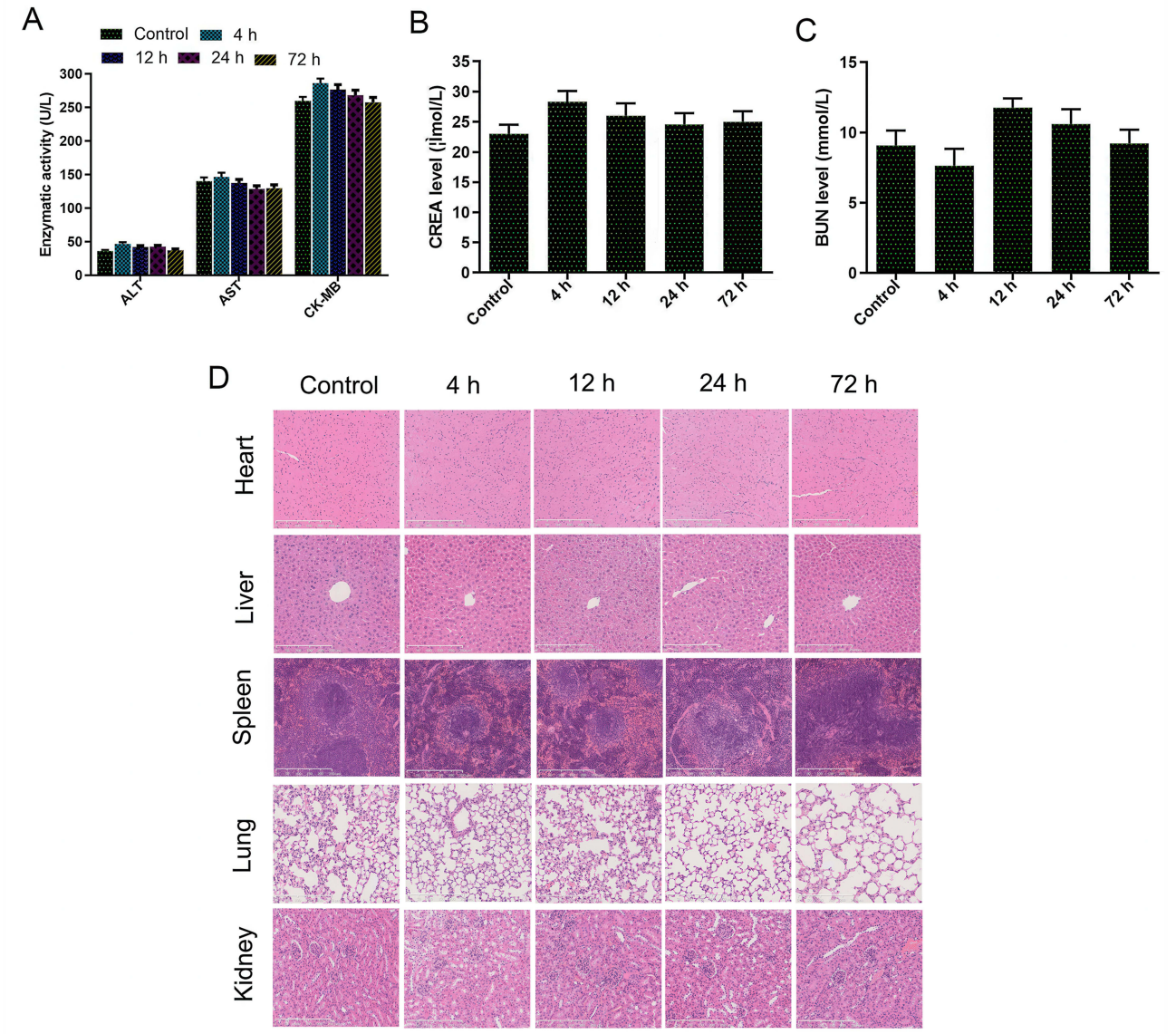

Figure 10 Safety verification of NCs in vivo. (**A**–**C**) Blood biochemistry was measured at different time points after intravenous injection of DNPA-aPD-L1 NCs in mice, with blood biochemistry from untreated mice serving as the control. (**D**) Microscopic images of H&E-stained tissues from various organs (×400 magnification). Treatment group: Mouse samples were obtained from the DNPA-aPD-L1 NCs group in the tumor treatment experiment.

observed in mice treated with the experimental group. These results indicate that, at the tested dose, targeted DNPA-aPD-L1 NCs do not induce any systemic toxicity or other physiological complications in vivo.

Discussion and Conclusion

TNBC is the most aggressive form of breast cancer, marked by high rates of early recurrence and metastasis and poor clinical outcomes. The immunosuppressed tumor microenvironment and the limited exposure of tumor-associated antigens in TNBC limit the efficacy of traditional treatment modalities (chemotherapy and surgery). Consequently, the development of more effective treatment strategies is imperative. In this study, we developed a novel nanoscale drug delivery platform (DNPA-aPD-L1 NCs) with a core composed of PLGA, AuNPs as the shell, encapsulating the chemotherapy drug DOX and the IDO inhibitor NLG919, and externally modified with PD-L1 antibody. PLGA is among the most prevalent and effective nanocarriers in the domain of nanomedicine research.[37] Drug-loaded PLGA demonstrates pH responsiveness and photothermal responsiveness, thereby establishing a foundation for controlled drug

release.[38] Furthermore, gold NCs demonstrate a high photothermal conversion efficiency within the near-infrared region, leading to their extensive utilization in photothermal therapy for tumors.[39] In comparison with chemotherapy, gold nanoparticle-mediated PTT offers several advantages, including a reduced treatment duration, the ability to be repeated, low toxicity, and the absence of drug resistance. It has been demonstrated that drug-loaded PLGA gold shell-coated NCs, when exposed to near-infrared laser irradiation, exhibit the capability to combine sustained-release and light-controlled drug release.

This combination effectively overcomes the "peak-trough" phenomenon,[40] thereby maintaining stable drug concentrations in the body. Gold's properties in the NIR region render it suitable for PAI. PAI is a non-invasive imaging technique that combines the principles of optical and ultrasound imaging, thereby enabling high-resolution visualization of internal tissue structures. In recent years, its application in cancer treatment has increased significantly.[41] At present, the diagnosis and treatment of TNBC face challenges due to a lack of specific imaging identification and therapeutic targets. This deficiency hinders the ability to identify cancerous tissue at the molecular level. Despite the occurrence of significant local tissue thermal damage caused by PTT, tumors persist in their ability to resist complete eradication. Furthermore, the inadequate immunogenicity of the tumors remains a significant impediment to effective control of recurrence and distant metastasis.[42] In a related study, Lin et al targeted the PD-L1 immune checkpoint using PD-L1-antibody-modified copolymer-structured nanodrugs, achieving effective inhibition of TNBC growth and lung metastasis. In our present study, the materials prepared exhibited excellent PAI performance, thereby enabling visualization-guided treatment of TNBC. Furthermore, DIR iodide was successfully encapsulated into NCs, and fluorescence imaging techniques were used to confirm the tissue distribution and peak time of NCs in vivo. The present findings demonstrate that PD-L1 can serve as an effective target for imaging and immunotherapy in TNBC.[43] DOX, when used as a first-line drug for the treatment of TNBC, has been shown to enhance antitumor immunogenicity by triggering the ICD effect. Consequently, the DOX-loaded NCs developed in this study have the capacity to selectively augment the ICD effect at tumor sites.[44] Furthermore, the combined effects of photothermal and chemotherapy therapy have been shown to remodel the immune microenvironment, thereby amplifying the antitumor and ICD effects of DOX. This observation is consistent with the experimental findings of our study. Primary TNBC tumors exhibited significant tumor necrosis, CRT and HMGB1 proteins levels after combined treatment with targeted drug-loaded microcapsules and laser therapy.

NLG919 has been demonstrated to be an effective inhibitor of indoleamine 2,3-dioxygenase, a key enzyme in the regulation of T cell proliferation and immune function. PD-L1 antibody has been shown to bind to PD-L1 on the surface of cancer cells, thereby blocking its interaction with PD-1 on T cells. This results in the inhibition of T cell exhaustion and the enhancement of the tumor-killing function of T cell immunity. To date, only a limited number of studies have validated the efficacy of IDO inhibitors in combination with aPD-L1 dual immune checkpoint therapy for TNBC.[45] Hu et al demonstrated that NLG919 exhibits synergistic effects with aPD-L1, and their combination achieves effective treatment for metastatic breast cancer. In our present study, In this study, after treatment in a metastatic tumor model, no signs of recurrence were observed at the primary tumor site in the group treated with NLG919-loaded targeted drugs + laser therapy, and the growth of metastatic lesions was significantly inhibited. Moreover, the results from whole-body in vivo fluorescence imaging, lung macroscopic specimens, and survival curves demonstrated the absence of obvious metastatic lesions in the lungs of this group, accompanied by a marked extension in survival. The rationale underlying this observation may be attributed to the dual immune checkpoint inhibition functions of DNPA- aPD-L1 NCs, which possess both IDO inhibitors and aPD-L1. The synergistic effects of these components have been demonstrated to significantly impede the recurrence and metastasis of TNBC.

This study successfully validated that the combination therapy strategy of photothermal therapy, chemotherapy, IDO inhibitors, and aPD-L1 dual immune checkpoint inhibition can achieve programmable synergistic sensitization therapy effects for TNBC using NCs that were prepared. To date, there have been no reports of a similar nature published in the academic literature.[46,47] Compared to other advanced nano-strategies, our DNPA-aPD-L1 NCs platform offers distinct advantages. Unlike composite systems like ZIF-8/AuNRs, the exposed gold nanoshell facilitates efficient antibody conjugation, resulting in superior active targeting and tumor accumulation, as validated by our in vivo imaging results. Furthermore, in contrast to erythrocyte-mimetic strategies that primarily enhance circulatory longevity, our active targeting via anti-PD-L1 not only promotes tumor-specific accumulation but also simultaneously instigates localized

immune checkpoint blockade, thereby synchronizing targeting and therapeutic functions within the tumor microenvironment.

Preliminary mechanistic experiments were conducted in our study, revealing that the combination of targeted NCs loading drugs and laser therapy increased the levels of HSP70, CRT, and HMGB1 proteins. These proteins have been shown to enhance the ability of immune cells to recognize tumor cells. Furthermore, we observed varying degrees of elevation in IFN-γ, IL-2, IL-12, and TNF-α cytokines in the spleen, indicating changes in the immune microenvironment following tumor treatment. These mechanisms may underlie the observed good positive outcomes. Finally, the results of the study confirmed that DNPA- aPD-L1 NCs are primarily metabolized by the liver, with a portion metabolized by the kidneys, and that gold NCs can be excreted within a short period. In vivo toxicity experiments further substantiated the safety profile of NCs.

However, although this study demonstrated the successful conjugation and retained functionality of the antibodies through both in vitro and in vivo experiments, future studies should focus on further optimizing the antibody conjugation efficiency to enhance its potential for clinical translation. In vivo experiments, the effects of NCs on activating the body's non-specific immune function and on ICD were assessed, without further analyzing the expression of immune regulatory molecules on T cell subsets and tumor cell surfaces or investigating their correlation with treatment efficacy. This was done to elucidate the mechanism by which combined therapy induces programmed synergistic sensitization and killing of tumor cells, leading to long-lasting immune memory.

DNPA-aPD-L1 NCs developed in our study possess light-triggered photochemotherapy capabilities that effectively induce ICD, enhance tumor immunogenicity, inhibit IDO activity and alleviate immune suppression in the tumor microenvironment. Therefore, this programmatic therapeutic regimen exhibits synergistic effects, enhancing the body's sensitivity to the treatment of primary TNBC lesions and effectively preventing tumor recurrence and metastasis. In addition, these novel NCs have the ability to visualize and localize TNBC tissue at the molecular level, thereby guiding in vitro near-infrared laser irradiation for photothermal therapy and chemotherapy. This method offers significant advantages in clinical applications, enabling precise, visualized, and guided treatment for TNBC. The "all-in-one" multifunctional platform developed by our study directly addresses core challenges in TNBC clinical translation—including the lack of effective targets, treatment resistance, and high recurrence/metastasis rates—by organically integrating diagnosis with therapy, and local physical killing with systemic immune activation. More significantly, this system demonstrates excellent biosafety, and each of its components has an established foundation for independent clinical use. This provides compelling feasibility evidence and a clear development pathway for its ultimate clinical translation.

In conclusion, the photochemotherapy mediated by the DNPA-aPD-L1 NCs we developed, combined with tumor microenvironment remodeling and immune activation, shows great promise for the diagnosis and treatment of TNBC.

Author Contributions

All authors made a significant contribution to the work reported, whether that is in the conception, study design, execution, acquisition of data, analysis and interpretation, or in all these areas; took part in drafting, revising or critically reviewing the article; gave final approval of the version to be published; have agreed on the journal to which the article has been submitted; and agree to be accountable for all aspects of the work.

Funding

This study was supported by the National Natural Science Foundation of China (Grant No. 82071954).

Disclosure

The authors report no conflicts of interest for this work.

References

1. Keenan TE, Tolaney SM. Role of immunotherapy in triple-negative breast cancer. *J Natl Compr Canc Netw*. 2020;18(4):479–489. doi:10.6004/jnccn.2020.7554

2. Obidiro O, Battogtokh G, Akala EO. Triple negative breast cancer treatment options and limitations: future outlook. *Pharmaceutics*. 2023;15(7):1796. doi:10.3390/pharmaceutics15071796
3. Lee J. Current treatment landscape for early triple-negative breast cancer (TNBC). *J Clin Med*. 2023;12(4):1524. doi:10.3390/jcm12041524
4. Zagami P, Carey LA. Triple negative breast cancer: pitfalls and progress. *NPJ Breast Cancer*. 2022;8(1):95. doi:10.1038/s41523-022-00468-0
5. Overchuk M, Weersink RA, Wilson BC, Zheng G. Photodynamic and photothermal therapies: synergy opportunities for nanomedicine. *ACS Nano*. 2023;17(9):7979–8003. doi:10.1021/acsnano.3c00891
6. Liu S, Pan X, Liu H. Two-dimensional nanomaterials for photothermal therapy. *Angew Chem Int Ed Engl*. 2020;59(15):5890–5900. doi:10.1002/anie.201911477
7. Yang JK, Kwon H, Kim S. Recent advances in light-triggered cancer immunotherapy. *J Mater Chem B*. 2024;12(11):2650–2669. doi:10.1039/d3tb02842a
8. Li Z, Lai X, Fu S, et al. Immunogenic cell death activates the tumor immune microenvironment to boost the immunotherapy efficiency. *Adv Sci*. 2022;9(22):e2201734. doi:10.1002/advs.202201734
9. Yi J, Liu L, Gao W, et al. Advances and perspectives in phototherapy-based combination therapy for cancer treatment. *J Mater Chem B*. 2024;12(26):6285–6304. doi:10.1039/d4tb00483c
10. Hu H, Zhao J, Ma K, et al. Sonodynamic therapy combined with phototherapy: novel synergistic strategy with superior efficacy for antitumor and antiinfection therapy. *J Control Release*. 2023;359:188–205. doi:10.1016/j.jconrel.2023.05.041
11. Zhang P, Wu Q, Yang J, et al. Tumor microenvironment-responsive nanohybrid for hypoxia amelioration with photodynamic and near-infrared II photothermal combination therapy. *Acta Biomater*. 2022;146:450–464. doi:10.1016/j.actbio.2022.04.044
12. Alamdari SG, Amini M, Jalilzadeh N, et al. Recent advances in nanoparticle-based photothermal therapy for breast cancer. *J Control Release*. 2022;349:269–303. doi:10.1016/j.jconrel.2022.06.050
13. Li Z, Sun L, Lan J, et al. Illuminating the fight against breast cancer: preparation and visualized photothermal therapy of hyaluronic acid coated ZIF-8 loading with indocyanine green and cryptotanshinone for triple-negative breast cancer. *Mater Today Bio*. 2024;28:101200. doi:10.1016/j.mtbio.2024.101200
14. Li X, Lovell JF, Yoon J, et al. Clinical development and potential of photothermal and photodynamic therapies for cancer. *Nat Rev Clin Oncol*. 2020;17(11):657–674. doi:10.1038/s41571-020-0410-2
15. Xiao Y, Zhu T, Zeng Q, et al. Functionalized biomimetic nanoparticles combining programmed death-1/programmed death-ligand 1 blockade with photothermal ablation for enhanced colorectal cancer immunotherapy. *Acta Biomater*. 2023;157:451–466. doi:10.1016/j.actbio.2022.11.043
16. Wang Y, Chen Y, Ji DK, et al. Bio-orthogonal click chemistry strategy for PD-L1-targeted imaging and pyroptosis-mediated chemo-immunotherapy of triple-negative breast cancer. *J Nanobiotechnology*. 2024;22(1):461. PMID: 39090622. doi:10.1186/s12951-024-02727-7
17. Park M, Lim J, Lee S, et al. Nanoparticle-mediated explosive anti-PD-L1 factory built in tumor for advanced immunotherapy. *Adv Mater*. 2025;37(7):2417735. doi:10.1002/adma.202417735
18. Hu T, Zhang L, Lu Y, et al. Biohybrids of anoxia-targeted bacteria/MDPP for enabling targeted synergistic immunotherapy and chemotherapy against breast tumors. *Int J Nanomedicine*. 2025;20:6813–6829. doi:10.2147/IJN.S515213
19. Wang X, Jing ZQ, Huang XB, et al. PD-L1 antibody conjugated dihydrotanshinone I-loaded polymeric nanoparticle for targeted cancer immunotherapy combining PD-L1 blockade with immunogenic cell death. *Int J Pharmaceut*. 2024;667(Pt B):125004. doi:10.1016/j.ijpharm.2024.125004
20. Qian X, Yang H, Ye Z, et al. Celecoxib augments paclitaxel-induced immunogenic cell death in triple-negative breast cancer. *ACS Nano*. 2024;18(24):15864–15877. doi:10.1021/acsnano.4c02947
21. Du M, Wang T, Peng W, Feng R, Goh M, Chen Z. Bacteria-driven nanosonosensitizer delivery system for enhanced breast cancer treatment through sonodynamic therapy-induced immunogenic cell death. *J Nanobiotechnology*. 2024;22(1):167. doi:10.1186/s12951-024-02437-0
22. Liang J, Tian X, Zhou M, et al. Shikonin and chitosan-silver nanoparticles synergize against triple-negative breast cancer through RIPK3-triggered necroptotic immunogenic cell death. *Biomaterials*. 2024;309:122608. doi:10.1016/j.biomaterials.2024.122608
23. Lin D, Lv W, Qian M, et al. Engineering cell membrane-camouflaged COF-based nanosatellite for enhanced tumor-targeted photothermal chemoimmunotherapy. *Biomaterials*. 2025;314:122869. doi:10.1016/j.biomaterials.2024.122869
24. Chen Z, Zhang Q, Huang Q, et al. Photothermal MnO nanoparticles boost chemo-photothermal therapy-induced immunogenic cell death in tumor immunotherapy. *Int J Pharm*. 2022;617:121578. doi:10.1016/j.ijpharm.2022.121578
25. Fujiwara Y, Kato S, Nesline MK, et al. Indoleamine 2,3-dioxygenase (IDO) inhibitors and cancer immunotherapy. *Cancer Treat Rev*. 2022;110:102461. doi:10.1016/j.ctrv.2022.102461
26. Charehjoo A, Majidpoor J, Mortezaee K. Indoleamine 2,3-dioxygenase 1 in circumventing checkpoint inhibitor responses: updated. *Int Immunopharmacol*. 2023;118:110032. doi:10.1016/j.intimp.2023.110032
27. Zheng D, Wan C, Yang H, et al. Her2-targeted multifunctional nano-theranostic platform mediates tumor microenvironment remodeling and immune activation for breast cancer treatment. *Int J Nanomed*. 2020;15:10007–10028. doi:10.2147/IJN.S271213
28. Zhang M, Shao S, Yue H, et al. High stability Au NPs: from design to application in nanomedicine. *Int J Nanomed*. 2021;16:6067–6094. doi:10.2147/IJN.S322900
29. Liu D, Liu L, Liu F, Zhang M, Wei P, Yi T. HOCl-activated aggregation of gold nanoparticles for multimodality therapy of tumors. *Adv Sci*. 2021;8(17):e2100074. doi:10.1002/advs.202100074
30. Sun H, Wang T, Ma W, et al. A stable DNA Tetrahedra-AuNCs nanohybrid: on-site programmed disassembly for tumor imaging and combination therapy. *Biomaterials*. 2022;288:121738. doi:10.1016/j.biomaterials.2022.121738
31. Wang Z, He L, Che S, et al. AuNCs-LHRHa nano-system for FL/CT dual-mode imaging and photothermal therapy of targeted prostate cancer. *J Mater Chem B*. 2022;10(27):5182–5190. doi:10.1039/d2tb00531j
32. Mao W, Kim HS, Son YJ, Kim SR, Yoo HS. Doxorubicin encapsulated clicked gold nanoparticle clusters exhibiting tumor-specific disassembly for enhanced tumor localization and computerized tomographic imaging. *J Control Release*. 2018;269:52–62. doi:10.1016/j.jconrel.2017.11.003
33. Wu CY, Hsieh HH, Chang TY, et al. Development of MRI-detectable boron-containing gold nanoparticle-encapsulated biodegradable polymeric matrix for boron neutron capture therapy (BNCT). *Int J Mol Sci*. 2021;22(15):8050. doi:10.3390/ijms22158050
34. Song Q, Wang D, Li H, et al. Dual-response of multi-functional microsphere system to ultrasound and microenvironment for enhanced bone defect treatment. *Bioact Mater*. 2023;32:304–318. doi:10.1016/j.bioactmat.2023.10.007

35. Huang C, Yang X, Li H, et al. GSH-responsive polymeric micelles-based augmented photoimmunotherapy synergized with PD-1 blockade for eliciting robust antitumor immunity against colon tumor. *J Nanobiotechnology*. 2024;22(1):542. Erratum in: *J Nanobiotechnology*. 2024;22(1):624. doi: 10.1186/s12951-024-02899-2. doi:10.1186/s12951-024-02813-w
36. Jiang H, Zhou Y, Zheng D, et al. Using anti-PD-L1 antibody conjugated gold nanoshelled poly (Lactic-co-glycolic acid) nanocapsules loaded with doxorubicin: a theranostic agent for ultrasound imaging and photothermal/chemo combination therapy of triple negative breast cancer. *J Biomed Mater Res*. 2024;112(3):402–420. doi:10.1002/jbm.a.37638
37. Su Y, Zhang B, Sun R, et al. PLGA-based biodegradable microspheres in drug delivery: recent advances in research and application. *Drug Deliv*. 2021;28(1):1397–1418. doi:10.1080/10717544.2021.1938756
38. Pinho S, Coelho JMP, Gaspar MM, Reis CP. Advances in localized prostate cancer: a special focus on photothermal therapy. *Eur J Pharmacol*. 2024;983:176982. doi:10.1016/j.ejphar.2024.176982
39. Alle M, Sharma G, Lee SH, Kim JC. Next-generation engineered nanogold for multimodal cancer therapy and imaging: a clinical perspectives. *J Nanobiotechnology*. 2022;20(1):222. doi:10.1186/s12951-022-01402-z
40. Delgado-Corrales BJ, Chopra V, Chauhan G. Gold nanostars and nanourchins for enhanced photothermal therapy, bioimaging, and theranostics. *J Mater Chem B*. 2025;13(2):399–428. doi:10.1039/d4tb01420k
41. Sharifi M, Attar F, Saboury AA, et al. Plasmonic gold nanoparticles: optical manipulation, imaging, drug delivery and therapy. *J Control Release*. 2019;311–312:170–189. doi:10.1016/j.jconrel.2019.08.032
42. Lin M, Cai Y, Chen G, et al. A hierarchical tumor-targeting strategy for eliciting potent antitumor immunity against triple negative breast cancer. *Biomaterials*. 2023;296:122067. doi:10.1016/j.biomaterials.2023.122067
43. Ma X, Yang S, Zhang T, et al. Bioresponsive immune-booster-based prodrug nanogel for cancer immunotherapy. *Acta Pharm Sin B*. 2022;12 (1):451–466. doi:10.1016/j.apsb.2021.05.016
44. Han R, Liu Q, Lu Y. Lu Y, et al.Tumor microenvironment-responsive AgS-PAsp(DOX)-cRGD nanoparticles-mediated photochemotherapy enhances the immune response to tumor therapy. *Biomaterials*. 2022;281:121328. doi:10.1016/j.biomaterials.2021.121328
45. Hu C, Song Y, Zhang Y, et al. Sequential delivery of PD-1/PD-L1 blockade peptide and IDO inhibitor for immunosuppressive microenvironment remodeling *via* an MMP-2 responsive dual-targeting liposome. *Acta Pharm Sin B*. 2023;13(5):2176–2187. doi:10.1016/j.apsb.2023.02.009
46. Yu Y, Zhang J, Huang W, et al. SunSpatiotemporally controlled AuNPs@ZIF-8 based nanocarriers for synergistic photothermal/chemodynamic therapy. *Acta Biomater*. 2023;317–328.
47. Dai J, Wu M, Wang Q, et al. Red blood cell membrane-camouflaged nanoparticles loaded with AIEgen and Poly(I: c) for enhanced tumoral photodynamic-immunotherapy. *Natl Sci Rev*. 2021;8(6):nwab039. doi:10.1093/nsr/nwab039